Oxygen Reduction Reaction on Doped Lanthanum Chromate Perovskites

by

Xinran Liu

A thesis
presented to the University of Waterloo
in fulfillment of the
thesis requirement for the degree of
Master of Science
in
Chemistry

Waterloo, Ontario, Canada, 2023

Author's Declaration

I hereby declare that I am the sole author of this thesis. This is a true copy of the thesis, including any required final revisions, as accepted by my examiners. I understand that my thesis may be made electronically available to the public.

Abstract

The oxygen reduction reaction (ORR) plays a pivotal role in fuel cell technology and the generation of clean oxidizing agents. This reaction can proceed via two distinct pathways. The complete ORR pathway involves reducing oxygen to water through a four-electron transfer process. Alternatively, a two-electron transfer pathway leads to the partial reduction of oxygen, yielding hydrogen peroxide (H_2O_2) as the product. The perovskite $CaSnO_3$ has demonstrated stability and selectivity in electrochemically oxidizing H_2O to H_2O_2. In a similar vein, other perovskite oxides have demonstrated good selectivity in the complete ORR. Their catalytic performance can be analyzed through microkinetic analysis and the application of scaling relations. In this study, we explore a series of perovskites based on $LaMO_3$, where 'M' denotes a combination of Cr, Co, and Ni. Changes in the type and concentration of doping lead to contraction in the perovskite lattice, along with alterations in B-O-B bond length and angle. These structural changes contribute to differences in their catalytic performance towards the ORR. The inclusion of Co in the catalyst tends to favor the four-electron ORR pathway, while the addition of Ni shows a predilection for the two-electron pathway.

Acknowledgements

I would like to thank my supervisor Prof. Rodney Smith, for his trust, guidance, and support throughout my M.Sc. program. He gave me this opportunity to work on this project and provide opportunities to explore other interesting topics and techniques. I have been learning a lot from his knowledge and his approach to science.

I would also like to express my gratitude to my committee members, Professor Anna Klinkova and Professor Vivek Maheshwari for their valuable time and advice over the past two years.

My appreciation also goes out to all the past and present members of our group: Dr. Alex Whittingham and Dr. Elif Pınar Alsac, Emily Yip, Dr.Holly Fruehwald, Keenan Black-Araujo, Una Hogan, Dr.Viswanathan Mohandoss, and Dr. Yutong Liu. Special thanks to Jixi Zhang and Ludan Zhu for their companionship and support.

Finally, none of this could have happened without my parents love and support. Thank you for giving me the courage and confidence to overcome all challenges and pursue an academic path far from home. This accomplishment would not have been possible without you.

Table of Contents

List of Figures

List of Tables

List of Abbreviations

EDXRF X-ray Fluorescence spectroscopy

FCEVs Fuel cell electric vehicles

HOR Hydrogen oxidation reaction

OER Oxygen evolution reaction

ORR Oxygen reduction reaction

PGMs Platinum-group metals

PXRD Powder X-ray diffraction

RHE Reversible hydrogen electrode

RRDE Rotating ring disk electrode

Chapter 1

Introduction

The oxygen reduction reaction (ORR) is a critical component in the development of clean energy technologies, with one of the most important applications being in fuel cell electric vehicles (FCEVs).[1,2] FCEVs represent a significant shift from traditional fossil fuel-based vehicles or those powered by battery-stored electrical energy, as they are fueled by hydrogen and emit only water and heat as byproducts. The efficiency of FCEVs is primarily attributed to the electrochemical reactions they utilize: the anodic hydrogen oxidation reaction (HOR) and the cathodic oxygen reduction reaction (**Figure 1.1**).[3,4] Despite rapid advancements in FCEV technology, challenges remain, particularly concerning the performance of fuel cell catalysts. Recent studies have significantly enhanced the catalytic performance of the HOR, making the exchange current of HOR reaction to be orders of magnitude higher than that of the ORR half-reaction.[5] The catalyst for the ORR has become a critical bottleneck in further improving fuel cell efficiency.

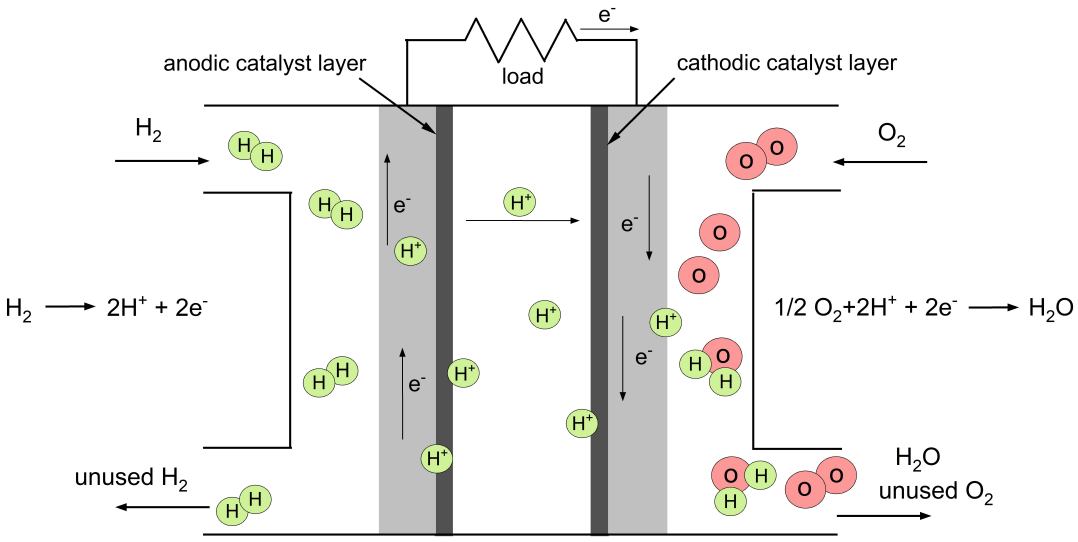

Figure 1.1: A schematic illustration of one type of electrolyte membrane fuel cell.

Conventional catalysts, predominantly those incorporating platinum-group metals (PGMs), are recognized for their superior efficiency in ORR. However, the high costs associated with PGMs present a significant limitation.[6] Consequently, there is an escalating interest in investigating alternative catalysts, especially traditional metal oxides that exclude platinum.[7,8] These alternatives are not only more cost-effective but also potentially offer enhanced durability compared to metal and metal alloy catalysts. Consequently, there is an increasing demand for research that merges theoretical and experimental methodologies with the aim of designing and elucidating the behavior of innovative metal oxide catalysts.

Hydrogen peroxide (H_2O_2) plays a pivotal role as an intermediate product in ORR and is extensively utilized as a clean oxidizing agent in both laboratory and industrial contexts.[9–12] Despite its various applications, the current production capacity of H_2O_2 is inadequate to meet the escalating global demand.[13,14] In industrial settings, H_2O_2 is produced through the anthraquinone reduction/oxidation process.[15] An alternative approach involves the on-site direct synthesis of H_2O_2 from hydrogen (H_2) and oxygen (O_2).[16] However, these approaches have limitations including low production efficiency, elevated costs, and notable safety hazards, which impede their scalability and widespread application. Electrochemical synthesis offers a more economical and environmentally friendly option for producing H_2O_2 from O_2. Recent

advancements, as depicted in **Figure 1.2**, demonstrate significant progress in enhancing the generation rate of H_2O_2 through modification of element combination in metal oxide catalysts.[17]

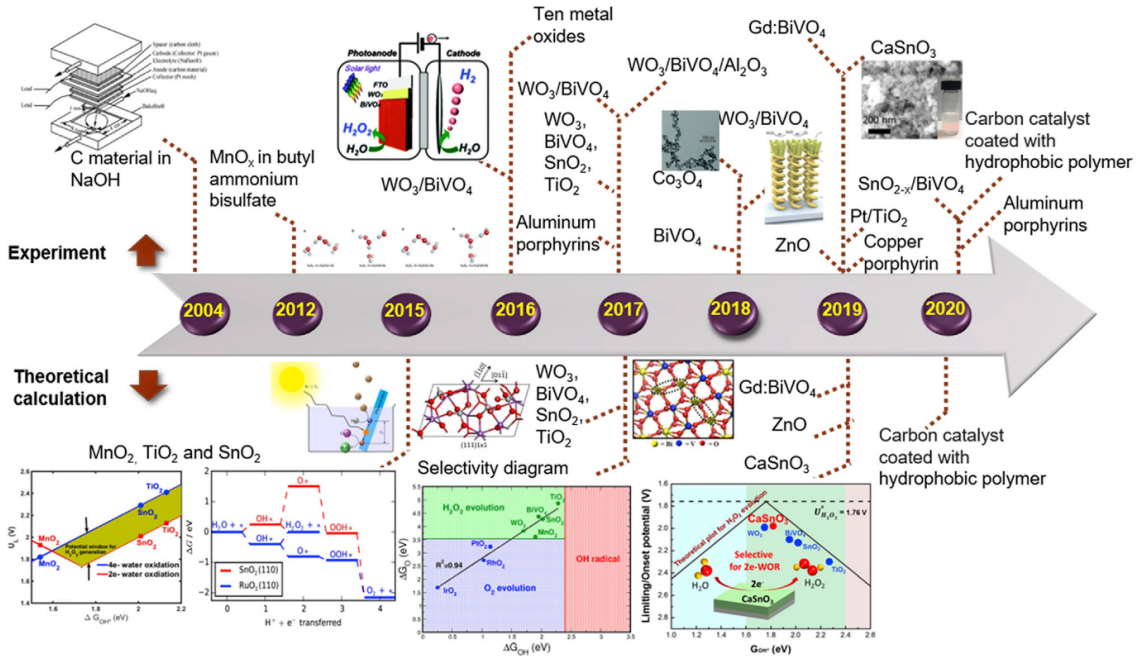

Figure 1.2: Previous research on two-electron water oxidation reaction for H_2O_2 production. Reproduced from [17] with permission.

The potential of metal oxides as catalysts in the sequential steps of ORR has garnered considerable interest in the field of electrochemistry and energy conversion. Within these reactions, metal oxides play a versatile role by facilitating multiple steps, including the reduction of oxygen to water (a four-electron process), or to hydrogen peroxide (a two-electron process). Owing to these divergent pathways, the selectivity of metal oxide catalysts emerges as a crucial factor. Consequently, a deeper understanding and improvement of the selectivity of these catalysts are required for optimizing their effectiveness in the corresponding reactions.

1.1 Oxygen reduction reaction

In the oxygen reduction reaction, molecular oxygen undergoes a reduction process, leading to the formation of either water or hydrogen peroxide with the loss of elec-

trons. The overall reactions can be represented as follows

four-electron step:

$$O_2 + H_2O + 4e^- \rightarrow 4OH^-(E^o = 1.23V) \tag{1.1}$$

two-electron step:

$$O_2 + 2H_2O + 2e^- \rightarrow H_2O_2 + 2OH^-(E^o = 0.70V) \tag{1.2}$$

Although the ORR reaction has been intensively studied, researchers haven't established a full understanding of the four electrons transfer mechanism. There are several proposed mechanism about the ORR reaction in alkaline media based on the different orientation of oxygen adsorption, like end-on adsorption, side-on adsorption, and bidentate adsorption mechanisms.[18,19] In here the end-on adsorption hypothesis was used as an example, which assumes that oxygen adsorbs strongly on a single B site of a perovskite oxide material to form a covalent bond (**Figure 1.3a**).[20] The reaction begins with the adsorption of oxygen molecules onto the catalyst's surface, leading to the formation of intermediate oxygen species. Subsequently, electron transfer occurs between these oxygen species and the active sites, which results in the cleavage of the O-O bond. Finally, the reaction products desorption happens from the catalyst surface, completing the process.

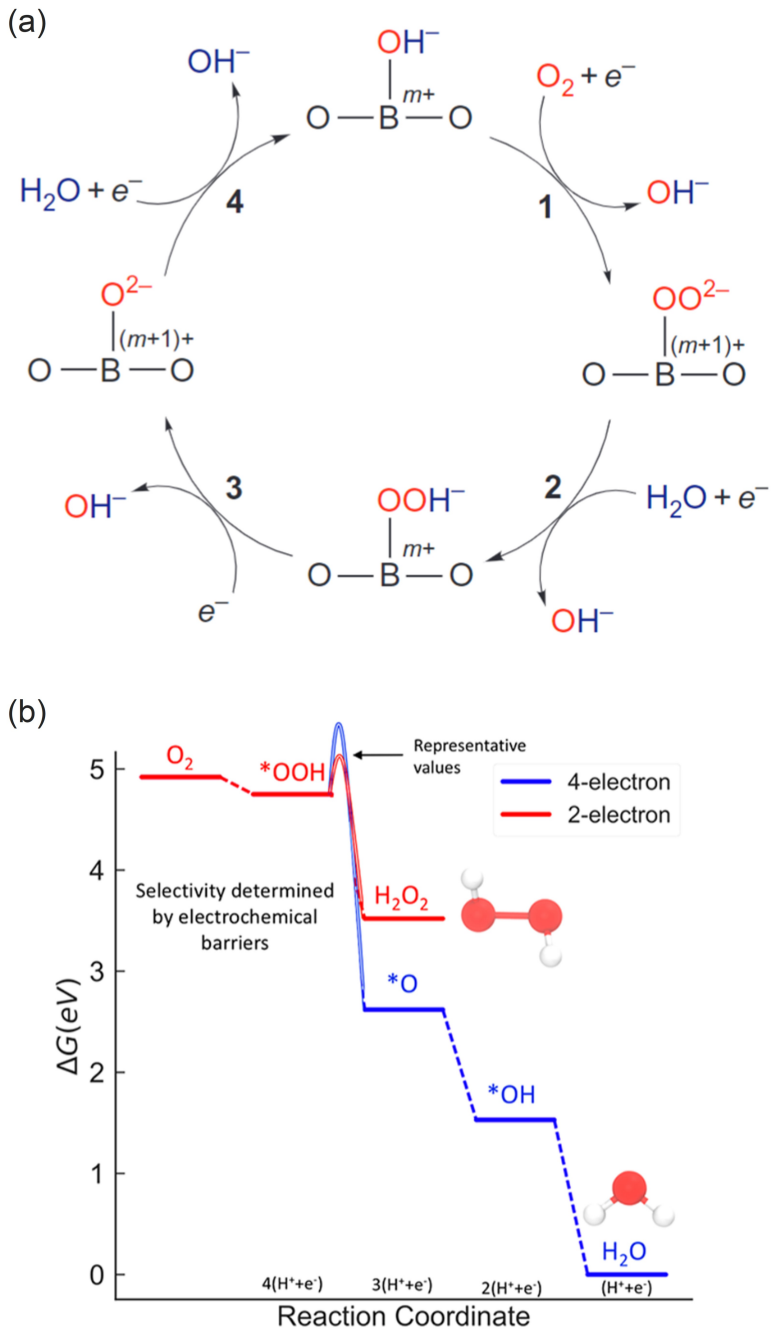

Figure 1.3: Oxygen reduction reaction mechanism. (a)Proposed ORR mechanism on perovskite oxide catalysts. Reproduced from [20] with permission. (b)Free energy diagram four the four- and two-electron ORR on Au(111). Reproduced from [21] with permission.

Previous studies have found that the dissociation of the O-O bond in the adsorbed OOH^* species is a critical determinant in ORR, dictating whether the reaction proceeds through a four-electron process to generate H_2O or a two-electron process to yield H_2O_2.[19,21] Specifically, catalysts with stronger oxygen binding en-

ergies, favoring the formation of O^* (indicated by a lower ΔG_{O^*}), lead the reaction along the pathway depicted as the blue path in **Figure 1.3b**. Conversely, catalysts with weaker binding to oxygen (characterized by a higher ΔG_{O^*}) tend to drive the reaction towards the formation of H_2O_2.

In the context of ORR, various oxygen species, including ΔG_{OOH^*}, ΔG_{O^*}, and ΔG_{OH^*}, are involved. Notably, their binding energies have been found to exhibit a linear relationship.[21] For example, **Figure 1.4** showed the calculated relationship between limiting potentials and the adsorption free energy of OH^* for the water oxidation reaction. Although this reaction is the reverse of the ORR, the underlying reaction logic remains consistent. For catalyst where ΔG_{OH^*} ranges approximately from 1.6 to 2.4 eV, the evolution of H_2O_2 is favored. For ΔG_{OH^*} values outside this range, the reaction tends towards the generation of either oxygen or OH radical species. This relationship enables researchers to use a single binding energy as a descriptor to correlate the binding energy of catalysts with their ORR selectivity.

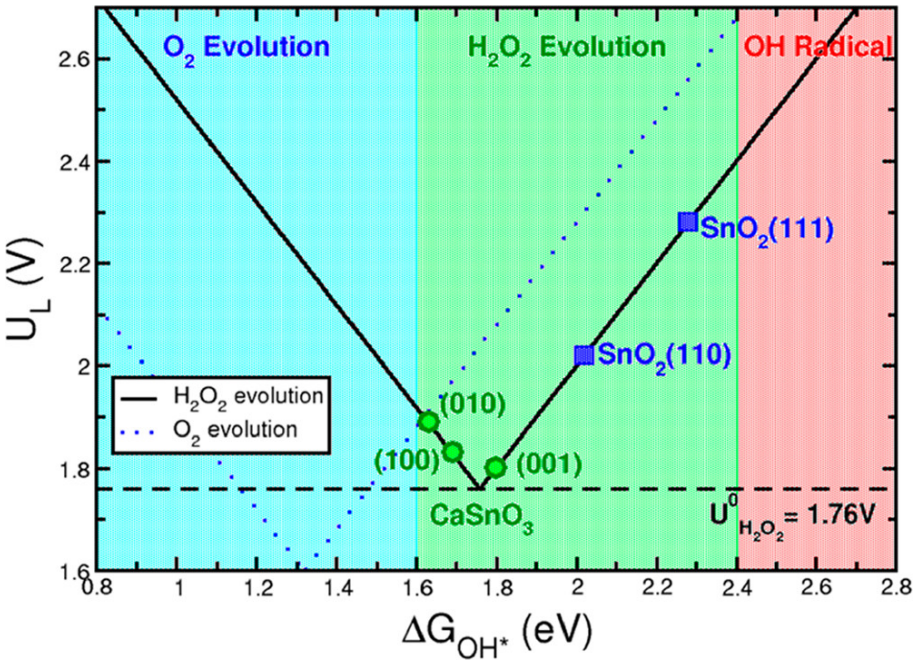

Figure 1.4: Theoretical activity volcano plots base on the calculated limiting potentials as a function of adsorption free energies of OH^*. Reproduced from [22] with permission.

1.2 Perovskite Oxide as catalyst for ORR reaction

1.2.1 Fundamentals about perovskite oxides

Perovskite was first identified in 1839 as a mineral with the chemical composition $CaTiO_3$, the name perovskite is in honor of the Russian mineralogist L.A. Perovski.[23] Subsequent research has expanded the term perovskite to encompass a broad family of compounds sharing structural similarities with $CaTiO_3$.[24] This extensive family includes various types of perovskites that have been the subject of extensive study, such as ABO_3 type perovskites, Ruddlesden-Popper layered perovskites (represented by the formula $A_{n+1}B_nO_{3n+1}$), A-site ordered double perovskite oxides ($AA'BO_6$), B-site ordered double perovskite oxides ($ABB'O_6$), and perovskite halides, among others.[18] A typical ABO_3 type perovskite structure exhibits a cubic or nearly cubic arrangement (**Figure 1.5a**). Within this lattice structure, the A-site cations are located at the cube's corners with a 12-fold coordination, while the B-site cations reside at the cube's center, forming an $[BO_6]$ polyhedron surrounded by oxygen atoms in a six-coordination setting. Generally, the A-site atoms are larger than the B-site atoms, serving as the structural framework of the lattice, with the B-site atoms and oxygen occupying specific interstitial positions.[25]

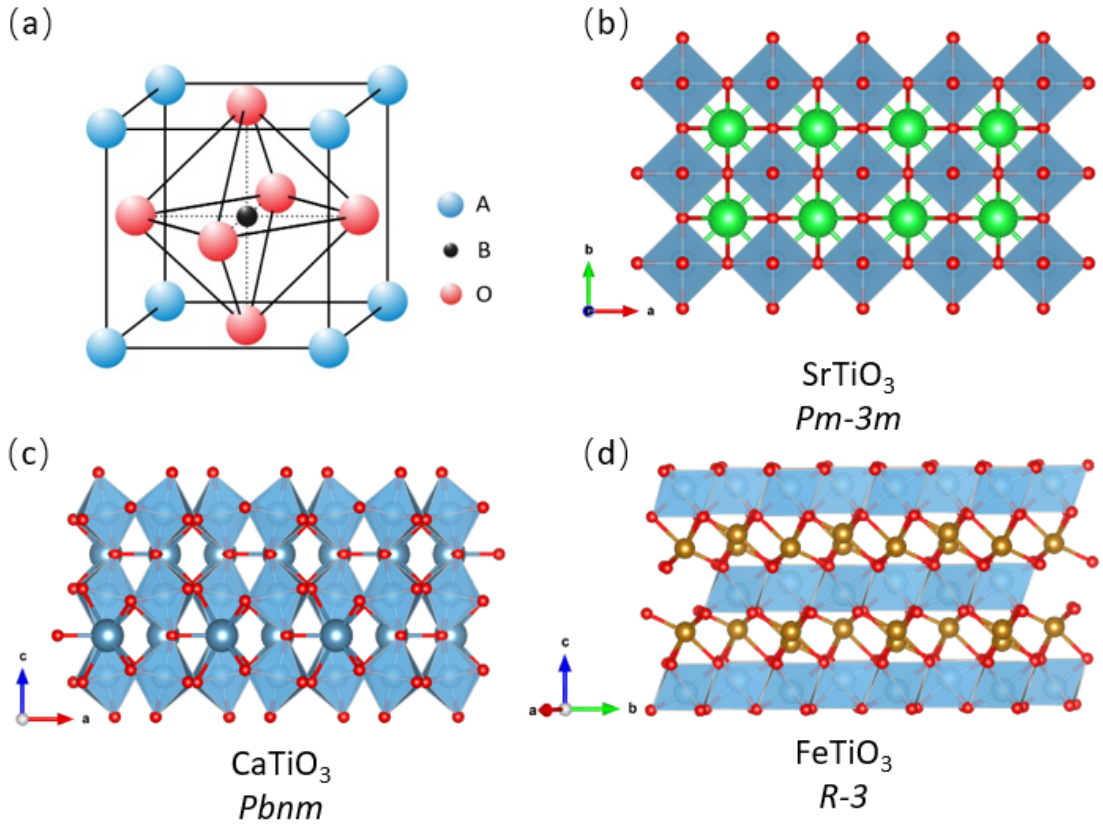

Figure 1.5: Examples of ABO_3 type of perovskites. (a) A schematic ABO_3 type of perovskite structure. Crystal structures of (b) $SrTiO_3$. (c) $CaTiO_3$. (d) $FeTiO_3$. Green spheres represent Sr atom, blue spheres represent Ca atom, gold spheres represent Fe atom. Blue polyhedral represents TiO_6 polyhedral structure.

The perovskite lattice undergoes structural distortions when different elements occupy the A-site or B-site, owing to the variance in atomic radii, which affects atom packing within the lattice. Several examples of these distortions are illustrated in **Figure 1.5**. For example, substituting the A-site Sr atom in $SrTiO_3$ with a smaller Ca atom results in lattice distortion. This substitution transforms the cubic structure of $SrTiO_3$ with $Pm\bar{3}m$ symmetry into an orthorhombic structure with $Pbnm$ symmetry. The $[BO_6]$ octahedra within the lattice become tilted due to this distortion. A more pronounced degree of distortion is observed when the A-site atom radius is further reduced, as seen in $FeTiO_3$, leading to a trigonal structure where the $[BO_6]$ octahedra share edges rather than corners.

Since the first synthesis of the perovskite oxide $LaCoO_3$ in the 1970s, there has been a significant expansion in the variety of perovskites synthesized, with respect to

the diverse cations occupying the A-site and B-site, and the exploration of their catalytic activities. As indicated in **Figure 1.6**, the range of elements commonly used in perovskite synthesis is quite extensive, encompassing most of the alkaline-earth and rare-earth metals for the A-site, and transition metals for the B-site. Beyond merely altering the A-site or B-site elements, these positions in the perovskite structure can also be substituted, and the concentration of the substituting material offers considerable flexibility. As discussed before, the changing of A or B cations lead to perovskite lattice distortion. This distortion is related to the stability and properties of the perovskite material. Consequently, it becomes essential to have a parameter that can describe the degree of this distortion within the perovskite lattice. Such a parameter would allow for a more systematic and quantitative understanding of how changes in lattice composition influence the material's physical and chemical properties, paving the way for tailored synthesis of perovskite materials for specific applications.

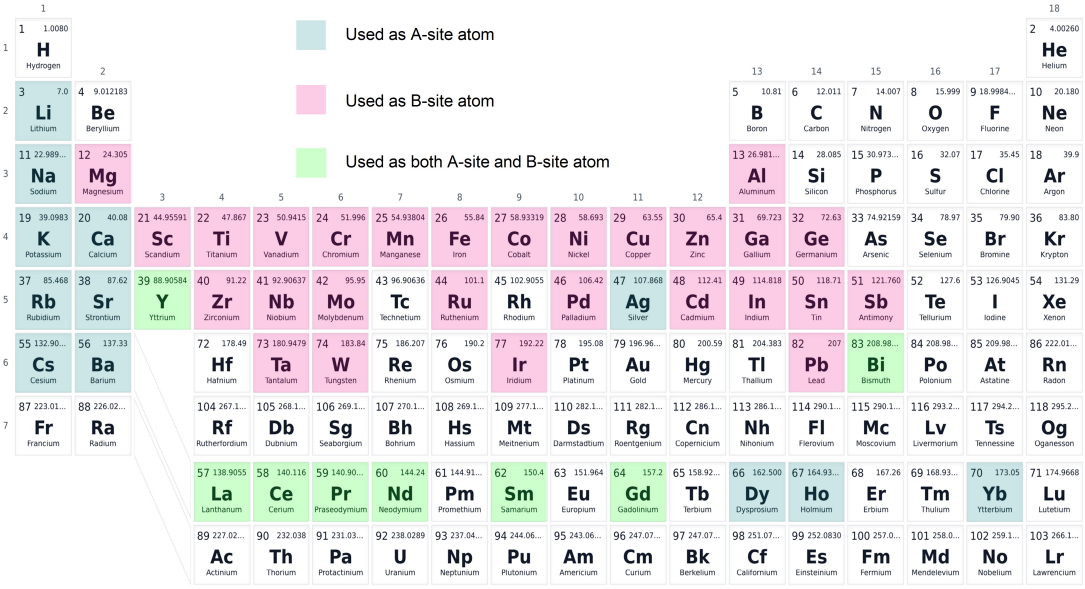

Figure 1.6: Common elements in the ABO_3 type of perovskite oxides.[18]

Goldschmidt's tolerance factor is a pivotal metric for assessing the stability and distortion of crystal structures. Initially formulated to describe the ABO_3 perovskite structure, the application of tolerance factors has since expanded to include other structures such as ilmenite.For the purposes of this project, which focuses on ABO_3

perovskites, the Goldschmidt tolerance factor is particularly apt for describing structural features induced by doping. In the formulation of Goldschmidt's tolerance factor, denoted as t equation, three key parameters are considered: r_{A}, r_{b}, and r_{O}. These represent the ionic radii of the A-site cation, B-site cation, and oxygen ion, respectively.[26] The tolerance factor is calculated using the following equation:

$$t = \frac{r_{\mathrm{A}} + r_{\mathrm{O}}}{\sqrt{2}(r_{\mathrm{B}} + r_{\mathrm{O}})} \tag{1.3}$$

In the specific context of this project, where doping occurs at the B-site, an adjusted tolerance factor equation becomes necessary to account for B-site doping in $AB_{1-x}B'_xO_3$ perovskites:

In the context of this project, doping atoms were introduced into the B-site position, an adjusted tolerance factor equation becomes necessary to account for B-site doping in $AB_{1-x}B'_xO_3$ perovskties[26] :

$$t = \frac{r_{\mathrm{A}} + r_{\mathrm{O}}}{\sqrt{2}[(1-x)r_{\mathrm{B}} + x r_{\mathrm{B'}} + r_{\mathrm{O}}]} \tag{1.4}$$

Theoretical tolerance factor values and their corresponding lattice structures are given in **Table 1.1**. The range of t in the table are guidelines rather than strict thresholds for space group transitions. A t value approximately between 0.9 and 1 suggests a cubic perovskite structure with ideally sized ions at both A-site and B-site positions. If t exceeds 1, it implies that the A-site ion is excessively large, or the B-site ion is too small. Tolerance factors between 0.71 and 0.9 indicate that the B-site ion is larger than ideal. When the tolerance factor drops below 0.71, a scenario more typical for ilmenite, the A-site and B-site ions are of similar radii, and the perovskite distorts into different structures, which falls outside the scope of this project. These guidelines assist in predicting the structural implications of various doping levels and combinations in perovskite materials.

Table 1.1: Tolerace factor value and their correspond structure[27]

tolerance factor (t)	Space group
>1.0	hexagonal/tetragonal
$\sim$ 0.9 to 1.0	cubic
0.71 to $\sim$ 0.9	orthorhombic/rhombohedral
<0.71	other structure

1.2.2 3d transition metals at perovsktie B-site

The first row of the transition metal region on the perodic table are elements with unfilled $3d$ shells as shown in **Table 1.2**. They have uncompleted d-subshell in their ground state, similar number of electrons and incorporate comparable chemical properties. From left to the right of the periodic table, electrons are added to the $3d$ elements' subshell under Aufau principle and Hund's rule with two important exceptions. Chromium has a $4s^1 3d^5$ electron configuration rather than the $4s^2 3d^4$ configuration predicted by the Aufbau principle, and copper is $4s^1 3d^{10}$ rather than $4s^2 2d^9$. These anomalies to the extra stability associated with half-filled subshells. The size of neutral atoms of the d-block elements gradually decreases from left to right across a row, due to an increase in the effective nuclear charge with increasing atomic number.

Table 1.2: Electron configurations of 3d transition metals

Sc	Ti	V	Cr	Mn
$4s^2 3d^1$	$4s^2 3d^2$	$4s^2 3d^3$	$4s^1 3d^5$	$4s^2 3d^5$
Fe	Co	Ni	Cu	Zn
$4s^2 3d^6$	$4s^2 3d^7$	$4s^2 3d^8$	$4s^1 3d^{10}$	$4s^2 3d^{10}$

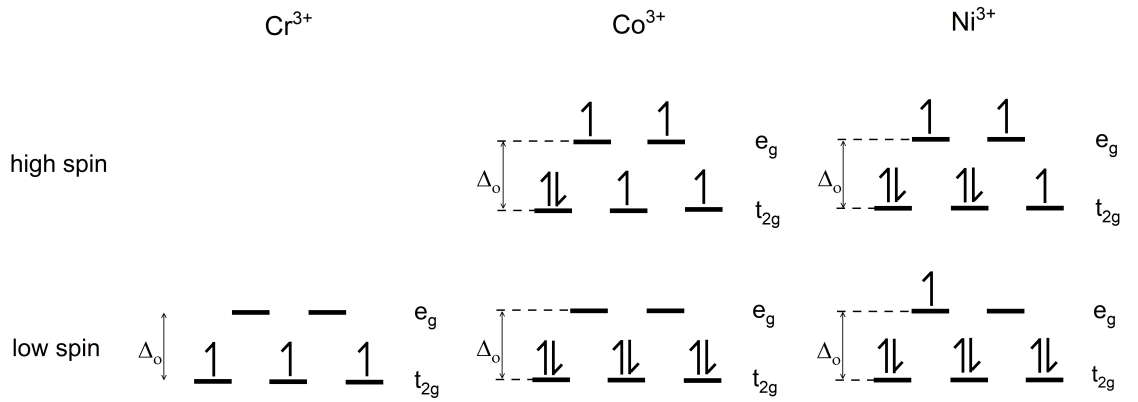

Figure 1.7: The 3d orbital configuration of Cr, Co, and Ni in their 3+ state.

In the ABO_3 perovsktie structurte, the B-site metal atom forms an $[BO_6]$ polyhedral with the surrounding oxygen, leading to the splitting of B-site atom's $3d$ orbital into e_g and t_{2g} orbitals (**Figure 1.7**). The $3d$ metal as B-site will have different orbital filling patterns according to their electron configurations and oxidation state. Previous studies have already show that ORR activity for perovskite oxides are related to the number of d-orbital electrons of B-site atoms.[20] **Figure 1.8a** showed that the maximun ORR activity was reached when the B-site atoms has d^4 or d^7 configurations. This activity trend is primarily effected by the number of electrons at the e_g orbital, which can be easily explained by the hybridization of B-site 3d orbitals and the oxygen $2p$ orbitals. As shown in **Figure 1.8b**, the circle shaped e_g orbital points directly towards the surrounding O atoms, leading to a stronger overlap between the B-site e_g orbitals and oxygen $2p$ orbitals, suggesting e_g rather than t_{2g} orbital of the B-ion should more accurately determine the energy of adsoption/desorption of oxygen, and thus effect the ORR activity if the adsorption/desorption process was involved in the rate-limiting step of ORR.

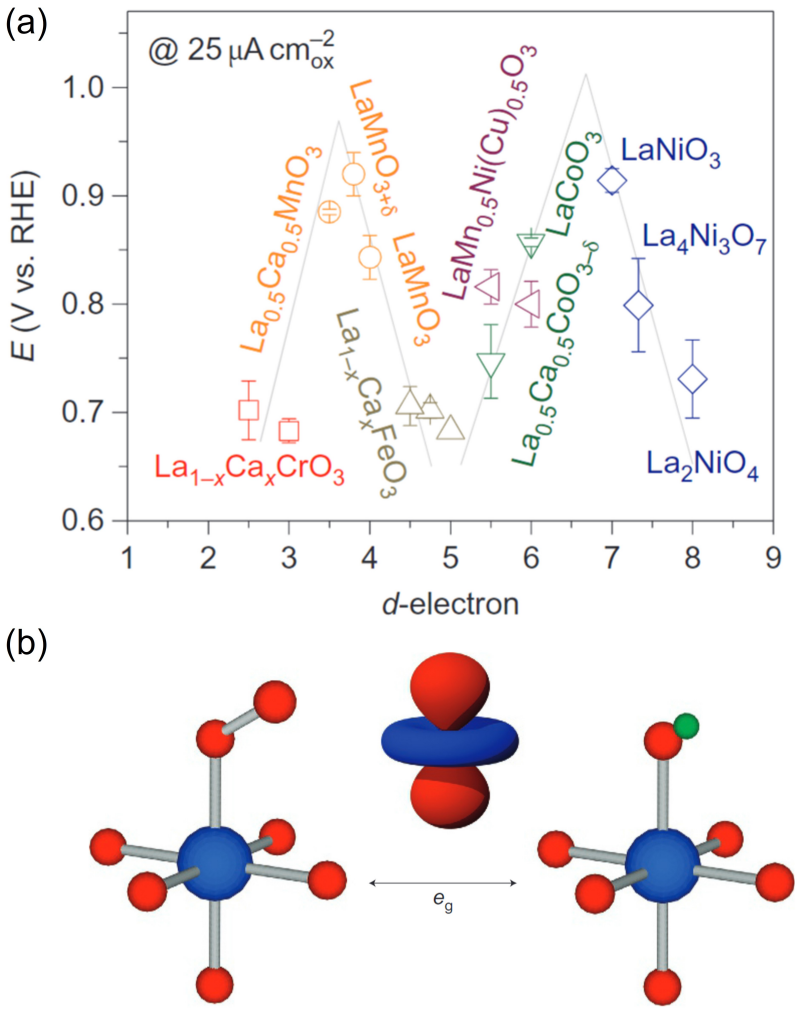

Figure 1.8: Role of d electrons on ORR activity of perovskite oxides. (a) Perovskite oxdies potentials in ORR reaction at 25 $\mu Acm^{-2}{}_{ox}$. (b) A schematic diagram of the e_g orbital of B-site atoms and the surrounding oxygen atoms. O,B and H atoms are coloured red, blue and green, respectively.Reproduced from [20] with permission.

1.3 Thesis Objective and Overview

The thesis investigates a series of perovskite materials based on $LaCr_xM_{1-x}O_3$, where M represents Ni or Co, to broaden the number of catalyst materials known to be capable of electrochemically catalyst ORR reaction. In **Chapter 1**, the motivation behind this thesis and the relevant background information are discussed. **Chapter 2** comprehensively details the theoretical and experimental methods employed throughout the project. **Chapter 3** focus on the characterization of $LaCr_xCo_{1-x}O_3$

and $LaCr_{1-x}Ni_xO_3$ series, exploring the impact of doping on the lattice structure. **Chapter 4** describes the experimental results in evaluating the catalytic performance for ORR reactions, and provides an overall discussion about the relationship between perovsktie doping and their catalytic performance. **Chapter 5** presents conclusions and future directions of this project.

Chapter 2

Material and Methods

2.1 Lanthanum Perovskite Oxide Synthesis

In this project, an adjusted Pechini method was used for sample synthesis.[28,29] A schematic procedure of the synthesis is shown in **Figure 2.1**. The synthesis starts in the aqueous phase, where 5mmol of La(III)$(NO_3)_3 \cdot 6H_2O$ (Thermo scientific, 99% REO) and a total amount of 5mmol transition metal nitrate, including Cr(III)$(NO_3)_3 \cdot 9H_2O$ (Acros Organics, 99%), Nickel(II)$(NO_3)_2 \cdot 6H_2O$ (Thermo scientific, 99% REO) or Co(II)$(NO_3)_2 \cdot 6H_2O$ (Alfa Aesar, 98.0-102.% ACS grade), were dissolved in water to form an aqueous phase. An excess amount (20mmol each) of anhydrous citric acid (fisher chemical, certified ACS) and ethylenediamine tetraacetic acid (EDTA) (fisher chemical, certified ACS) was added into the solution as chelating agents. The carboxylic group in citric acid and the polyamino carboxylic group in EDTA can bind the metal cations in the solution, ensuring an even distribution of metal ions in both the solution and the gel,[30,31] resulting in high purity products. The pH of the solution was then adjusted to 10 using NH_4OH (Sigma-Aldrich, ACS reagent, 28.0-30.0% NH_3 basis). The solution was then heated at 200°C on a heating plate to remove the nitrate and ammonia, causing the solution to condense and form a gel. Subsequently, the gel was combusted at 350°C to eliminate the organic components, transforming the gel into an ash precursor. In this project, all samples were synthesized by heating the precursors at 1000°C for 12 hours. After heating,

the samples were ground, and the heating procedure was repeated once.

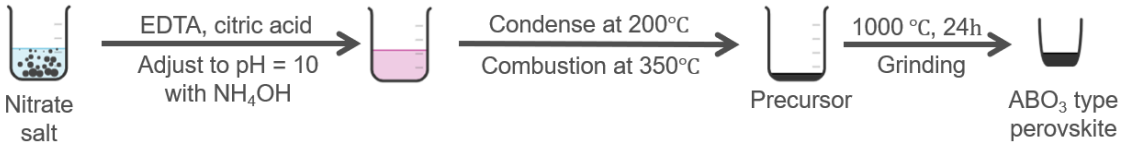

Figure 2.1: A schematic procedure of the synthesis of $LaCr_xNi_{1-x}O_3$ and $LaCr_xCo_{1-x}O_3$.

2.2 Material Characterization

2.2.1 Powder X-ray Diffraction

Powder X-ray diffraction (PXRD) experiments were performed at room temperature using an Inel XRG 3000 diffractometer with an aluminum sample holder. Each sample was measured for 15 minutes, and the structural information was analyzed by Rietveld refinement of the diffraction patterns using the GSAS-II software.[32]

2.2.2 Raman Spectroscopy

Raman spectroscopy was performed using a Renishaw inVia Reflex Raman microscope equipped with a 633 nm excitation laser and a 2400 lines/mm grating. Each measurement was obtained using 5% of the maximum intensity and an acquisition time of 600s. The acquired data were processed using Renishaw WiRE 5.5 software with operations including cosmic ray removal, baseline subtraction, and peak fit.

2.2.3 Energy Dispersive X-ray Flourescence Spectrometry

Energy dispersive X-ray fluorescence spectrometry (EDXRF) measurements were performed using a MiniPal4 benchtop spectrometer in a helium environment. Rhodium (Rh) was used as the tube anode, and aluminum was employed as the filter material. Each sample was measured four times at different energy levels (7 keV, 12 keV, 20

keV, and 30 keV) for better accuracy. The acquired data were exported from the MiniPal4 software and analyzed in Origin2020.

2.2.4 X-ray Absorption Spectroscopy

X-ray Absorption Spectroscopy (XAS) measurements were conducted at the 6-BM (BMM) beamline of the National Synchrotron Light Source II (Brookhaven National Laboratory). using a Si(111) monochromator. For the purpose of this study, the K-edge spectra of the B-site atoms were specifically collected in transmission mode. Three spectra were acquired per sample.

2.3 Electrochemical Techniques

2.3.1 Rotating ring disk electrode

In this project, a Metron Autolab was used to measure the electrochemical behavior of catalysts. As depicted in **Figure 4.1a**, the primary working electrode consists of a glass-carbon disk positioned at the center of the rotating ring disk electrode (RRDE). Surrounding the glass-carbon electrode is a platinum ring electrode, located at a distance of 375 μm, which functions as a secondary electrode for applying a fixed voltage. A plastic isolator material separates the disk and ring electrodes, as illustrated. For electrochemical measurements, the samples were spin-coated onto the glassy-carbon electrode. The RRDE electrode's rotation enables the transfer of electrolytic products generated at the disk electrode to the ring electrode for detection. Furthermore, the rotation induces convection near the surface of the RRDE, ensuring a constant thickness of the diffusion layer.[33] This process enables diffusion effects to be removed, allowing experiments to more reliably analyze kinetics.

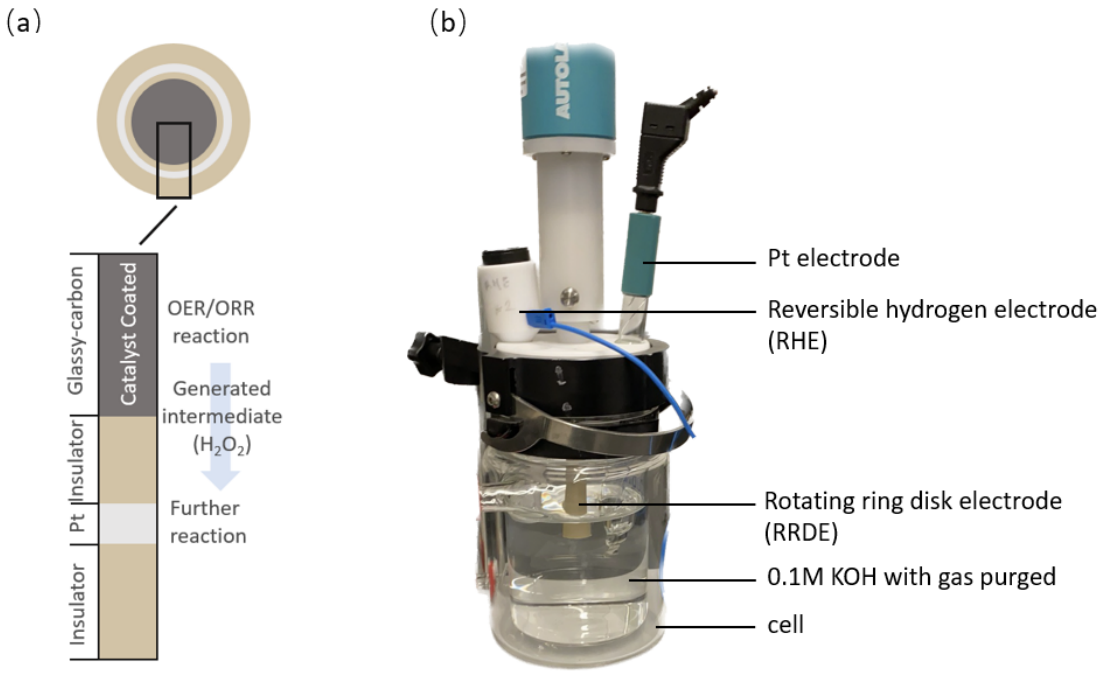

Figure 2.2: Electrochemical measurements setting. (a)A scheme of RRDE electrode (b) The three electrode system for electrochemical measurements.

A three-electrode system was used in this project, as shown in **Figure 2.2b**. A reversible hydrogen electrode (HydroFlex, Gaskatel GmbH) served as the reference electrode, and a platinum sheet electrode with a surface area approximately equal to 1 cm^2 (Metrohm, 3.109.0790) was employed as the counter electrode. All measurements were conducted using a Metrohm Autolab electrochemical workstation at a scan rate of 10mV·s^{-1}. The electrolyte used was 0.1M KOH, which was purged with O_2 for 15 min prior to use and maintained with a continuous gas flow during the measurements. Cyclic voltammetry(CV) measurements were performed with a voltage range from 0V to 1.4V without rotation. Linear sweep voltammetry(LSV) measurements were carried at a voltage range of 0 - 1.0V for the ORR reaction and 1.0 - 1.8V for the OER reaction, with rotation rates varying from 100 to 2400 revolutions per minute(rpm). Data was collected using Nova 2.1 software and exported to Origin 2020 for further analysis.

2.3.2 Preparation of coating suspension

The samples were initially ground with an agents mortar for 30 minutes to reduce the particle size. A 10 mg portion of the ground sample was mixed with 1.5 ml of a Nafion solution to create the coating suspension. The Nafion solution was prepared by first combining Nafion D-521 dispersion (Alfa Aesar, 5% w/w in water and 1-propanol, $\geq$0.92 meq/g exchange capacity) with the equal volume of 0.1M concentration of potassium hydroxide. The mixture is then diluted with ethanol in a 3:97 volumetric ratio to form the dilution solution. To ensure an evenly distributed suspension, the coating suspension with the samples was sonicated for 30 minutes. A 2.5 μl aliquot of the coating suspension was drop-cast onto a 5mm diameter glassy carbon disk electrode while the platinum ring was kept clean. The electrode was set to rotate at 900 rpm, and a heat gun directed towards the electrode surface for 90 seconds, using mild heating, to obtain a homogeneous and firm coating.

Chapter 3

The Impact of Cation Doping on the Perovskite Oxide Structure

3.1 Introduction

Perovskite oxides have a remarkable capacity to accommodate high concentrations of dopant elements, allowing tailored electrical and catalytic properties.[34,35] The [BO_6] polyhedral in the ABO_3 lattices are commonly connected via vertices, providing open paths for oxygen migration and affording ABO_3 perovskites with good catalytic activity. While both A-site and B-site doping influence the structure and consequent catalytic activity, B-site doping notably impacts perovskite catalytic properties, as supported by both theoretical calculations and experimental findings.[20,29,36] In ABO_3 perovskite with a tolerance factor (t) below 1, oxygen ion migration tends to depend more on the radius of B-site atoms rather than those at the A-site. Molecular orbital theory provides insight into how the d orbitals of B-site elements combine with the $2p$ orbital of oxygen, forming antibonding orbitals, further influencing catalytic activity. The electrons filling of B-site cations has a direct relationship with the catalytic activity of ABO_3 perovsktie oxides. The addition of dopants at the B-site induces structural alterations in the perovskite lattice, including lattice expansion in specific directions, oxygen defect variations, and shifts in B-O bond covalency, thus influencing electrochemical properties.[20,37,38]

The selection of $LaCrO_3$ as the starting point was driven by the stability of the Cr^{3+} state and its proven catalytic efficiency towards the four-electrons ORR.[38,39] Doping on the B-site, employing common $3d$ transition elements such as Co and Ni, was a focus of this study. The distinct electronic configurations of Co and Ni in different spin states influence the e_g orbital filling, leading to structural alterations in the perovskite lattice and varying adsorption abilities of oxygenated species on the B-site.

In this chapter, two lanthanum perovskite oxide series were studied, commencing with composition analysis and lattice structure determination. Subsequent analyses detailed the structural changes resulting from different types and concentrations of doping at the B-site.

3.2 Results

Within the framework of this research, two series of ABO_3 type perovskite oxides were synthesized using a modified sol-gel method. The chemical composition followed the formula $LaCr_{1-x}M_xO_3$, with M representing either Co or Ni, and x ranging from 0 to 1.0. The stoichiometry of A-site and B-site cations was maintained in a 1:1 ratio. Critical assessment and validation of the product composition and doping concentration were conducted via Energy-dispersive X-ray Fluorescence (EDXRF) spectroscopy. Because lanthanum at the A-site has a high atomic number, only the L peaks were detected, while chromium and cobalt, with low atomic value, exhibited K peaks in the spectra (**Figure 3.1a**). The intensity of the XRF peaks is proportional to the concentration of elements within the perovskite. The B-site doping concentration was evaluated through the analysis of both the $K_{\alpha 1}$ peaks and $K_{\beta 1}$ peaks. The experimental results showed good agreement with the intended values, indicating well-controlled doping of the sample and negligible contamination by extraneous elements.

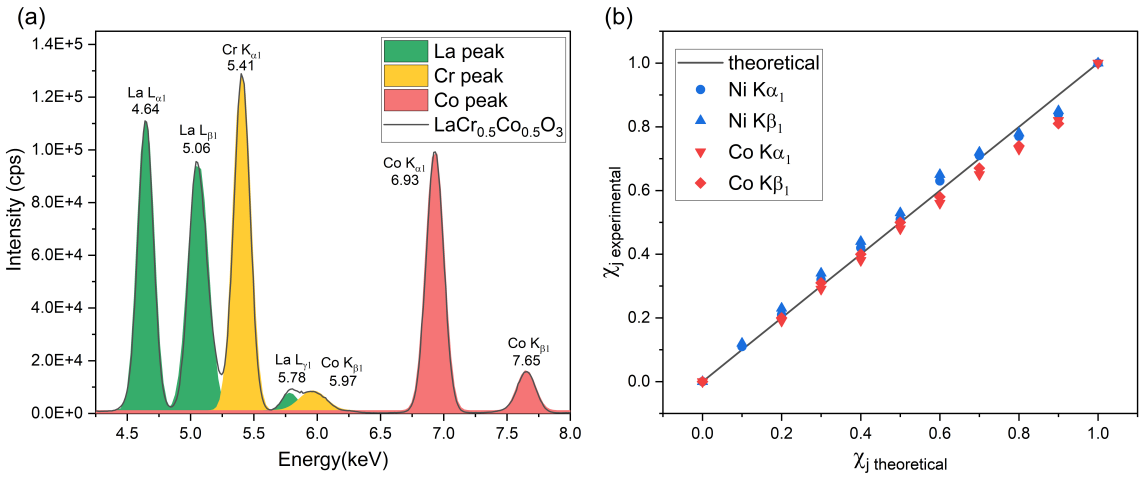

Figure 3.1: Energy-dispersive X-ray Fluorescence spectroscopy (EDXRF) analysis of the composition of the synthesized samples. (a) The results from Gaussian curve fitting for $LaCr_{0.5}Co_{0.5}$. (b) A comparison between the theoretical doping concentration and the calculated values for $LaCr_{1-x}Co_xO_3$ and $LaCr_{1-x}Ni_xO_3$ series. χ_j represents the doping concentration, where j = Co or Ni.

The PXRD spectra serve as a vital diagnostic tool for the analysis of perovskite structures. As the concentration of the metal dopant increases from 0 to 1.0, the PXRD spectra exhibit a clear separation into two distinct patterns, revealing a noteworthy phase transition (**Figure 3.2**). This transition is characterized by marked differences in peak intensities, particularly noticeable around a 2θ value of 47°, and the splitting of primary peaks at 34°, 41°, 54°, 59°, and 70°. These observations provide a means to confirm the perovskite structure through peak indexing. Matching the diffraction patterns to those expected for common perovskite phases indicates that the two observed phases are perovskites with the space groups $Pnma$ and $R\bar{3}C$. For Co-doped samples, the transition occurs from $R\bar{3}C$ to $Pnma$ when the amount of Co increase from 0.2 to 0.3. A similar trend is observed for Ni-doped samples, where the transition occurs at a higher doping concentration, specifically from 0.6 to 0.7.

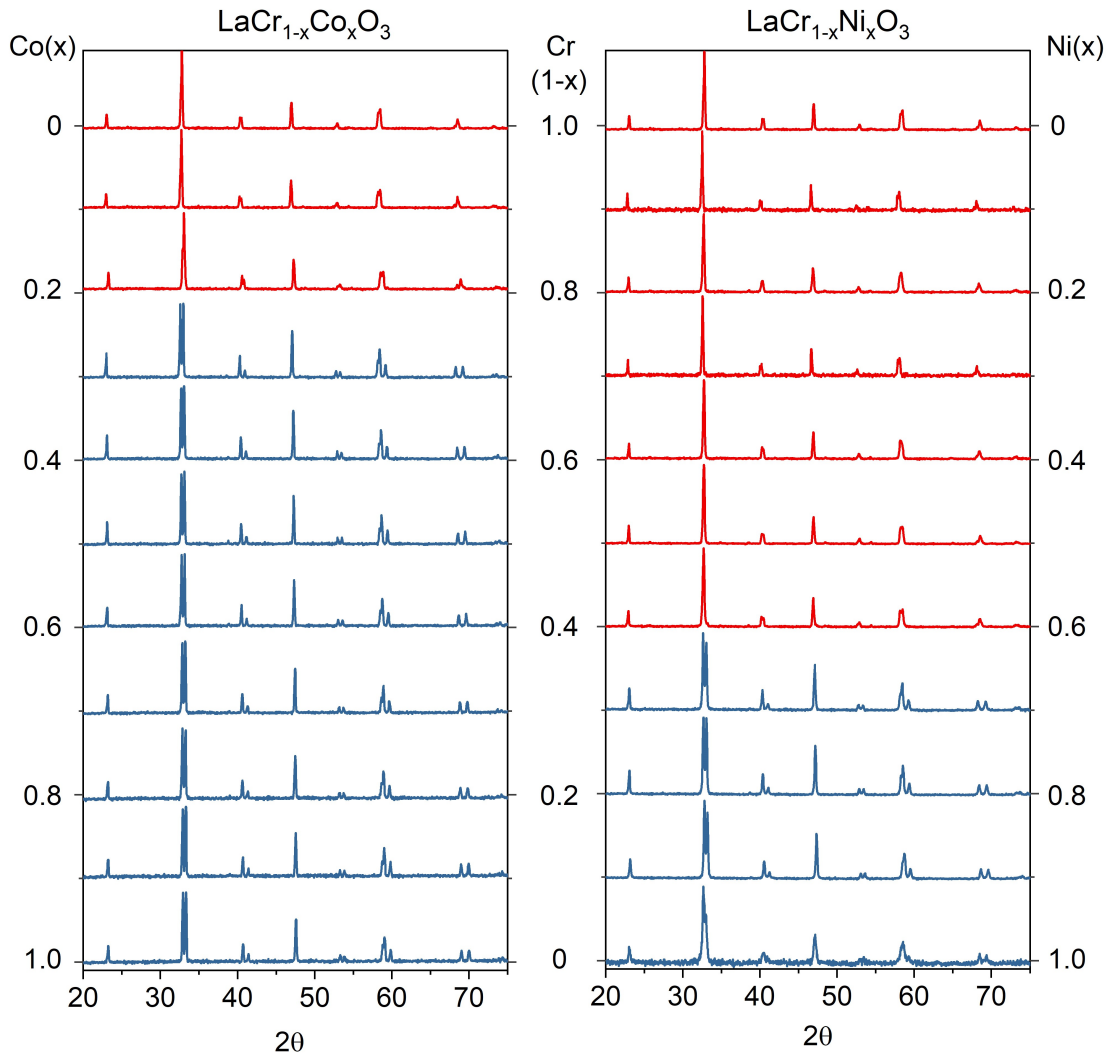

Figure 3.2: Powder X-ray diffraction spectra of $LaCr_xCo_{1-x}O_3$ and $LaCr_xNi_{1-x}O_3$ sample series. Red lines represent samples exhibiting a *Pnma* space group and blue lines an $R\bar{3}c$ space group.

The application of Rietveld refinement to the PXRD dataset has confirmed two distinct space groups associated with the synthesized perovskite oxides. Each sample exhibits consistency between the simulated and experimental peak patterns, with Δ/σ of less than ± 5 for all refinement results(**Figure 3.3**). This finding confirms the presence of a single-phase composition and high purity samples. Both the Co-doped and Ni-doped series exhibit a consistent trend in structural transition, wherein an increase in doping concentration leads to a transition from the *Pnma* space group to the $R\bar{3}c$ space group using Hermann-Mauguin notation. In this notation, the first symbol in the space group designates the Bravais lattice type, while the subsequent three parts describe the point group of the crystal. In the case of the *Pnma* space

group, P represents a primitive lattice, followed by descriptors indicating an n-glide plane along the x-axis, a mirror plane along the y-axis, and an a-glide plane along the z-axis. The $R\bar{3}c$ space group denotes a rhombohedral structure, with a 3-fold rotoinversion axis ($\bar{3}$), and a c-glide plane parallel to the rotoinversion axis (c). These distinctions in symmetry are evident through variations in naming of reflection planes, as illustrated by the hkl notation in **Figure 3.3**.

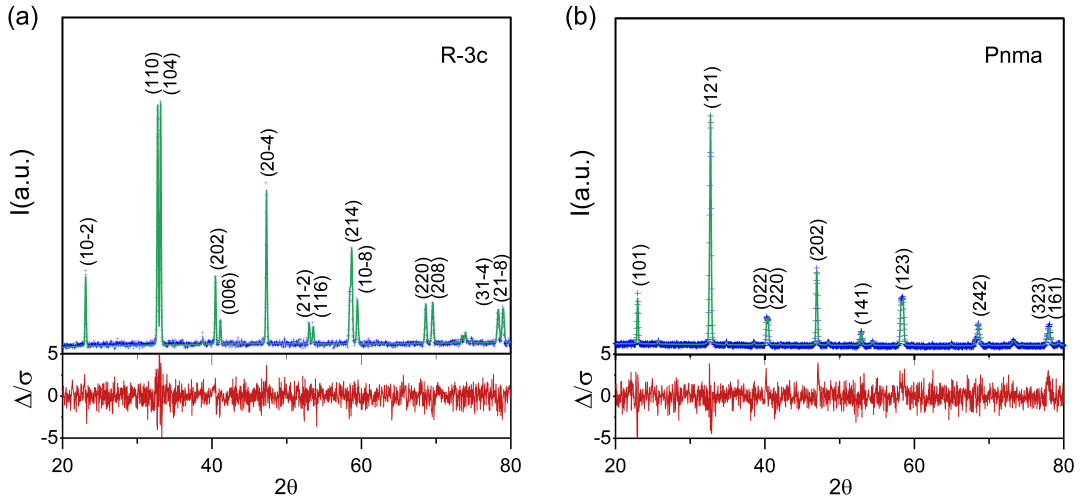

Figure 3.3: Rietveld refinement of $R\bar{3}c$ and $Pnma$ space group using (a) $LaCr_{0.5}Co_{0.5}O_3$ and (b) $LaCr_{0.5}Ni_{0.5}O_3$ respectively. Blue data points represent PXRD data, green lines represent refined XRD patterns, red lines represent the difference between data points and calculated value divided by an estimate of standard deviation in the measured intensity.

The lattice parameter data obtained from the Rietveld refinement is presented in **Table 3.1**. Parameters involved in the refinement were listed in **Table A.1**. It is essential to acknowledge that the two distinct space groups exhibit variations in the geometric arrangement of atoms, and as a result, the lattice axis parameters hold differing physical interpretations in these space groups. As delineated in **Figure 3.4c**, for the $Pnma$ space group, a and c correspond to the lattice axis parameters of the unit cell. In the case of the $R\bar{3}c$ space group, the situation is more complicated. There are correspondence between the $Pnma$ and $R\bar{3}c$ structure configurations. In the context of the [BO_6] polyhedral as our point of reference, it's noteworthy to recognize that the lattice plane denoted as $(10\bar{2})$ within the $R\bar{3}c$ space group corresponds to the (010) plane in the $Pnma$ structure. This correspondence is predicated on the fact that both of these planes are oriented perpendicular to the

layers of [BO_6] polyhedral. Similarly, the plane represented as (208) in the $R\bar{3}c$ space group corresponds to the (100) plane in the $Pnma$ structure, as both are oriented in parallel with the layers of [BO_6] polyhedral. In the subsequent discussions, parameter V is established as the distance between three adjacent (010) lattice layers within the $Pnma$ structure, and equivalently, the distance between three adjacent $(10\bar{2})$ layers within the $R\bar{3}c$ structure. Similarly, H is defined as the parameter indicating the distance between the three adjacent (100) lattice layers in the $Pnma$ structure, or alternatively, the distance between three adjacent (208) layers within the $R\bar{3}c$ structure.

In both Co-doped and Ni-doped series, an increase in doping concentration χ_j corresponds to a noticeable reduction in the lattice parameters V and H. As shown in **Figure 3.4a,b**, the transitions between different space groups within the doping series results in discrete changes in these parameters. When shifting from the $Pnma$ to the $R\bar{3}c$ structure, both V and H experience a increment. This phenomenon can be readily comprehended by considering the different arrangements of the A-site La and the [BO_6] polyhedral within the unit cell (**Figure 3.4c**). However, within the same space group, the lattice parameters V and H consistently decrease, signifying a reduction in the unit cell dimensions along all three lattice axes. The ratio of lattice parameters V/H indicates the lattice changes in magnitude of difference (**Figure 3.4d**). For Co-doped series, the V axis has a general trend of faster decreasing, the trend is more obvious for low Co composition samples that are in $Pnma$ structure. The trend is the same for Ni-doped series with $Pnma$ structure with fluctuations, while for the $R\bar{3}c$ samples the increase of doping have opposite trend to the lattice dimensions.

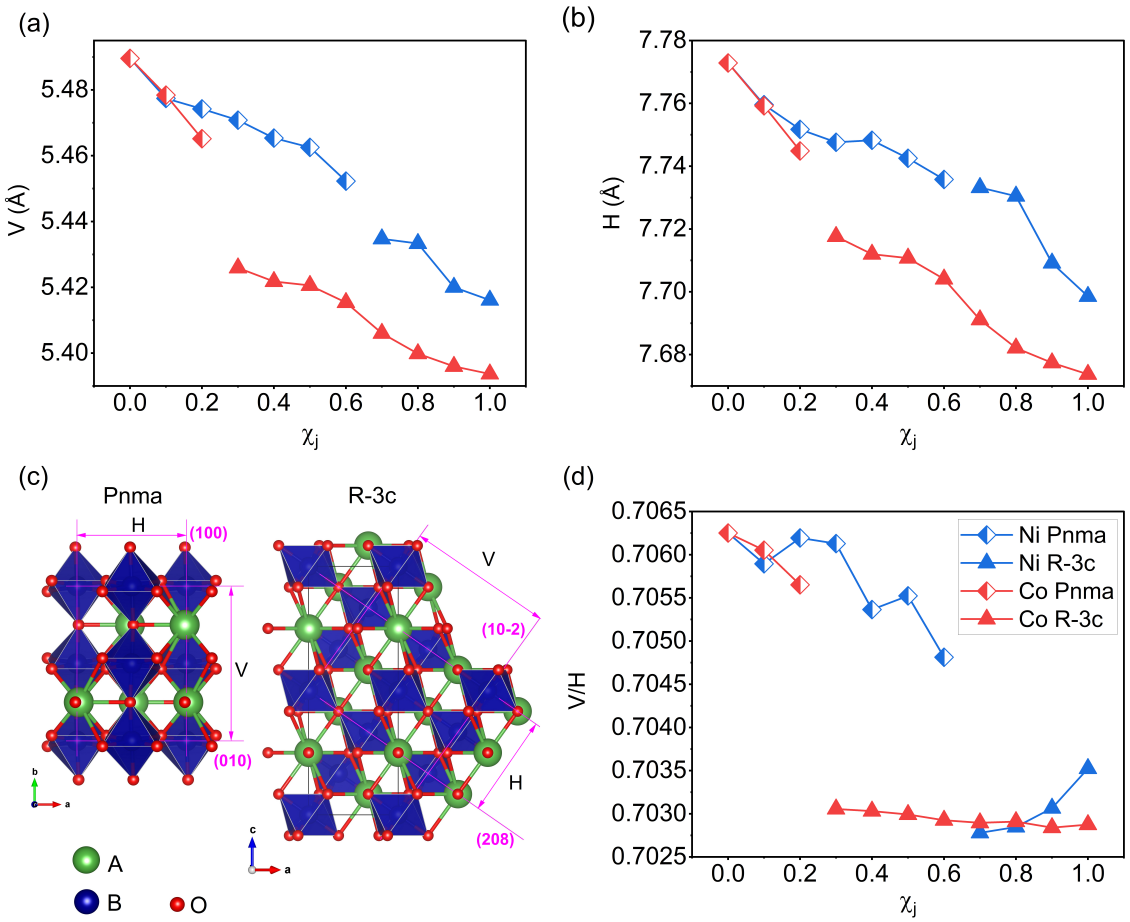

Figure 3.4: Unit cell parameters for $LaCr_{1-x}Co_xO_3$ and $LaCr_{1-x}Ni_xO_3$ (a) lattice layers internal distance V. (b) lattice layers internal distance H. (c) Example of *Pnma* and $R\bar{3}c$ lattices using the refined results of $LaCr_{0.5}Ni_{0.5}O_3$ and $LaCr_{0.5}Co_{0.5}O_3$.Unit cell (d) Parameter ratio for both series of samples.

Bond length and bond angle in the $[BO_6]$ polyhedral structure indicates the degree of distortion of the unit cell. The B-O-B bond angle and B-O bond length information is present in **Table 3.2**. In $R\bar{3}c$ space group, the $[BO_6]$ polyhedral has a regular octahedron structure, which has the same bond length of B-site atom to the oxygen atom in all directions. Within the unit cell, all the corner sharing octahedron has the same B-O-B bond angle. The *Pnma* structure has reduced symmetry compared to $R\bar{3}c$. The $[BO_6]$ polyhedron has different bond length for B-O_1, B-O_2, and B-O_3, where O_1, O_2, and O_3 indicate the oxygen atoms in different directions comparing to the central B-site atom (**Figure 3.5c**). The B-O-B bond angle in vertical (α_1) and horizontal (α_2) directions are also different, with a schematic illustration given in **Figure 3.5a**. Although the distortion in *Pnma* space group is

Table 3.1: Lattice parameters of $LaCr_{1-x}Co_xO_3$ and $LaCr_{1-x}Ni_xO_3$ phases.

Cr [1-x]	Co [x]	Space group	H (Å)	V (Å)	Volume (Å^3)
1.0	0.0	$Pnma$	5.490	7.773	235.8
0.9	0.1	$Pnma$	5.478	7.759	234.6
0.8	0.2	$Pnma$	5.465	7.745	233.2
0.7	0.3	$R\bar{3}c$	5.426	7.718	229.9
0.6	0.4	$R\bar{3}c$	5.422	7.712	229.4
0.5	0.5	$R\bar{3}c$	5.421	7.711	229.2
0.4	0.6	$R\bar{3}c$	5.415	7.704	228.6
0.3	0.7	$R\bar{3}c$	5.406	7.691	227.5
0.2	0.8	$R\bar{3}c$	5.400	7.682	226.7
0.1	0.9	$R\bar{3}c$	5.396	7.677	226.3
0.0	1.0	$R\bar{3}c$	5.394	7.674	226.0
Cr [1-x]	Ni [x]	Space group	H (Å)	V (Å)	Volume (Å^3)
1.0	0.0	$Pnma$	5.490	7.773	235.8
0.9	0.1	$Pnma$	5.477	7.760	234.2
0.8	0.2	$Pnma$	5.474	7.752	233.8
0.7	0.3	$Pnma$	5.471	7.748	233.3
0.6	0.4	$Pnma$	5.465	7.748	232.0
0.5	0.5	$Pnma$	5.463	7.743	232.7
0.4	0.6	$Pnma$	5.452	7.736	231.9
0.3	0.7	$R\bar{3}c$	5.435	7.733	231.3
0.2	0.8	$R\bar{3}c$	5.433	7.730	231.0
0.1	0.9	$R\bar{3}c$	5.420	7.709	229.1
0.0	1.0	$R\bar{3}c$	5.416	7.699	228.1

Table 3.2: Metal-oxygen bond parameters of $LaCr_{1-x}Co_xO_3$ and $LaCr_{1-x}Ni_xO_3$ phases.

Cr [1-x]	Co [x]	Space group	α_1 (°)	α_2 (°)	$B-O_1$ (Å)	$B-O_2$ (Å)	$B-O_3$ (Å)
1.0	0.0	$Pnma$	161.4	162.4	1.969	1.979	1.962
0.9	0.1	$Pnma$	159.2	160.8	1.972	1.974	1.969
0.8	0.2	$Pnma$	159.3	160.8	1.969	1.970	1.965
0.7	0.3	$R\bar{3}c$	164.3	-	1.948	-	-
0.6	0.4	$R\bar{3}c$	164.3	-	1.947	-	-
0.5	0.5	$R\bar{3}c$	164.3	-	1.946	-	-
0.4	0.6	$R\bar{3}c$	167.3	-	1.938	-	-
0.3	0.7	$R\bar{3}c$	167.3	-	1.935	-	-
0.2	0.8	$R\bar{3}c$	167.3	-	1.933	-	-
0.1	0.9	$R\bar{3}c$	167.3	-	1.931	-	-
0.0	1.0	$R\bar{3}c$	164.7	-	1.936	-	-
Cr [1-x]	Ni [x]	Space group	α_1 (°)	α_2 (°)	$B-O_1$ (Å)	$B-O_2$ (Å)	$B-O_3$ (Å)
1.0	0.0	$Pnma$	161.4	162.4	1.969	1.978	1.962
0.9	0.1	$Pnma$	159.3	160.8	1.972	1.972	1.968
0.8	0.2	$Pnma$	159.3	160.8	1.970	1.971	1.967
0.7	0.3	$Pnma$	159.3	160.8	1.969	1.970	1.966
0.6	0.4	$Pnma$	159.3	160.8	1.969	1.969	1.964
0.5	0.5	$Pnma$	159.2	160.8	1.968	1.969	1.964
0.4	0.6	$Pnma$	159.2	160.8	1.966	1.966	1.961
0.3	0.7	$R\bar{3}c$	162.2	-	1.957	-	-
0.2	0.8	$R\bar{3}c$	162.2	-	1.957	-	-
0.1	0.9	$R\bar{3}c$	162.2	-	1.951	-	-
0.0	1.0	$R\bar{3}c$	166.6	-	1.948	-	-

different in the three dimensions, they share the same trend and the numeric value differences are small. Based on the similarity, the B-O-B angle α_1 and bond length B-O_1 will be focused for analysis.

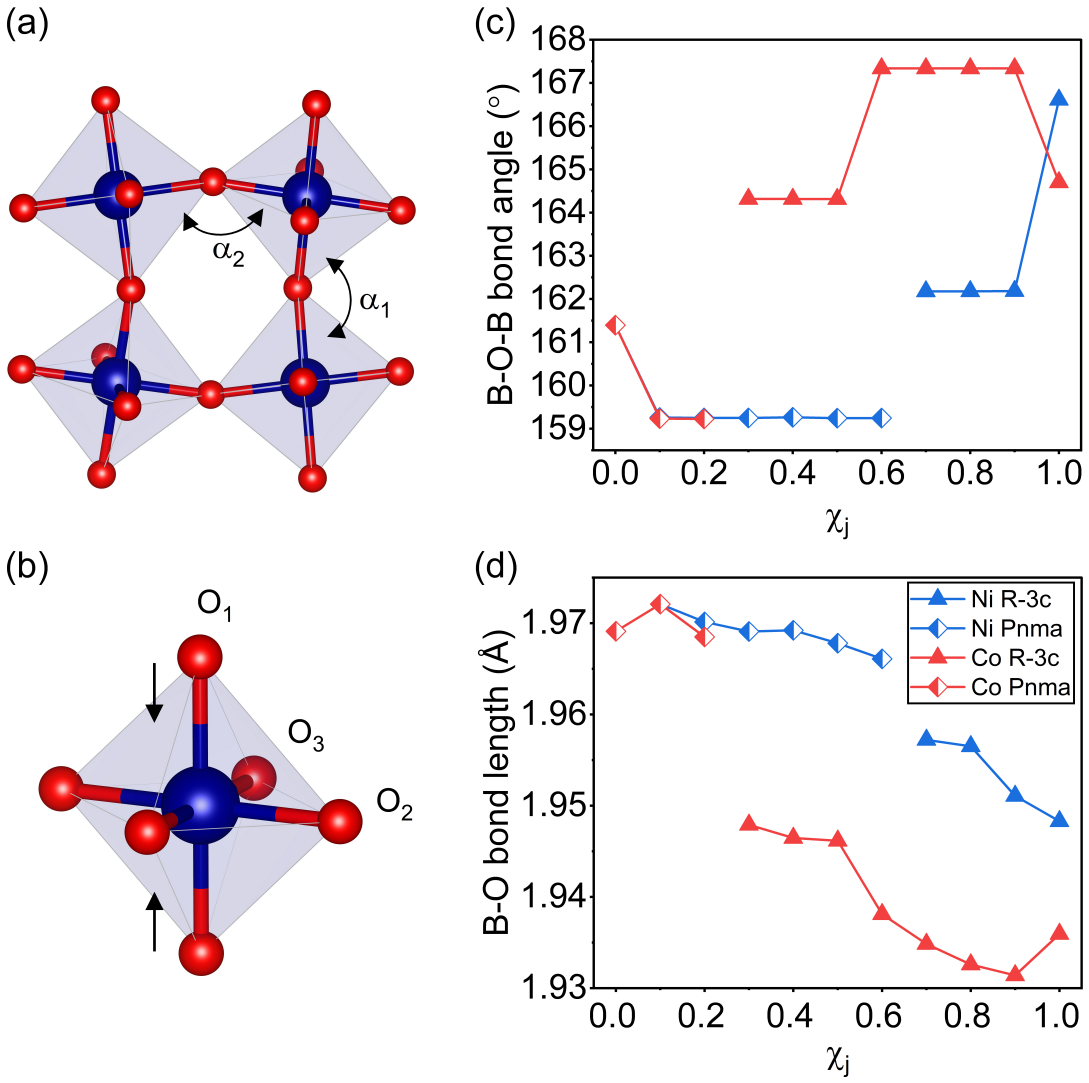

Figure 3.5: Analysis of B-O-B bond angle and bond length within the [BO_6] polyhedral. (a) A schematic illustration of B-O-B bond angles. (b) A schematic illustration of B-O bond notation. (c) A summary of bond angle and (d) B-O_1 bond length of the [BO_6] polyhedron within the lattice.

The B-O-B bond angle serves as an indicator of the degree of distortion within the unit cell. An angle equal to 180°represents the ideal cubic structure, with smaller bond angle indicating more significant distortion. During the transition from the *Pnma* to the $R\bar{3}c$ structure, the B-O-B bond angle had a substantial increase, indicating a reduction in structural distortion (**Figure 3.5c**). It is noteworthy that in the Co-doped perovskite, an increase in the B-O-B bond angle is evident

in the $R\bar{3}c$ phase, with the bond angle shifting from approximately 164.5°to around 167.5°when the doping concentration reaches 0.7 and above. This significant change is not observed in the Ni-doped series, where bond angle variations within the same space group are minor. Notably, the parent samples without doping do not follow the observed trend in bond angle changes. Concurrently, with an increase in B-site doping, the B-O_1 bond length consistently decreases in both series, indicating the contraction of the [BO_6] polyhedral within the unit cell (**Figure 3.5d**). Samples in the $R\bar{3}c$ structure exhibit shorter B-O_1 bond lengths compared to those in the *Pnma* structure, indicating a more compact polyhedral structure and stronger B-O bond.

An attempt to utilize Raman spectroscopy for structural analysis was undertaken as part of this research project. However, the regular octahedral arrangement of [BO_6] in the $R\bar{3}c$ and *Pnma* space group does not exhibit detectable B-O oscillations. In accordance with the Raman analysis from related studies (**Table 3.3**), Raman peaks indicative of [BO_6] are typically found in the 200 to 450 cm^{-1} region. However, the experimental data (**Figure 3.6**) does not exhibit consistent peaks within this rage that exhibit a clear trend. While the parent $LaCrO_3$ sample displays a pristine spectrum, this trend is not maintained upon the introduction of doping. For Ni-doped series with χ_{Ni} ranging from 0.7 to 1.0, which adopt the $R\bar{3}c$ structure, a broad peak is observed around 400 cm^{-1}. In accordance with **Table 3.3**, this peak is attributed to the bending of [BO_6] octahedra. Notably, this peak is absent in the Ni-doped samples with the *Pnma* structure. The peak undergoes a red shift followed by a blue shift with increasing doping, indicating variations in the strength of the B-O bond. There are also spectra feature peaks around 350, 430, and 500 cm^{-1} which cannot be attributed to B-O oscillations, as they lack consistency across the series. These spikes are likely a result of the low polynomial number used for data analysis(4 in this project), which can cause certain background noise to resemble Raman peaks.

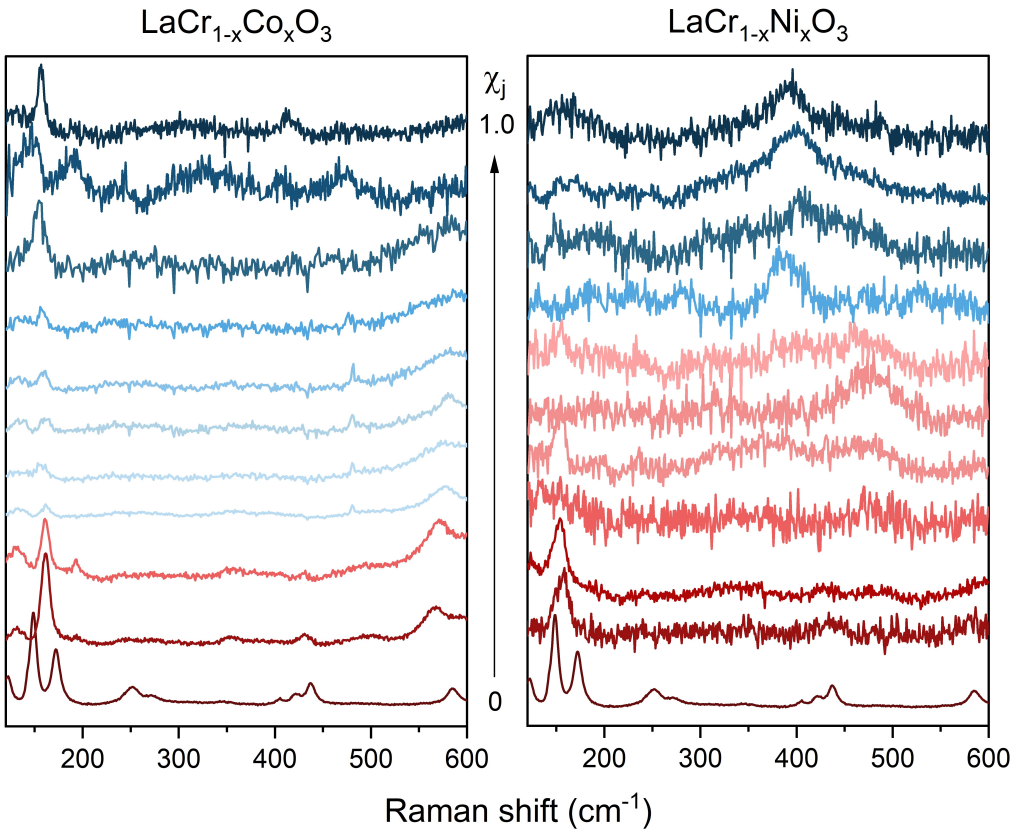

Figure 3.6: Raman spectra of $LaCr_{1-x}Co_xO_3$ and $LaCr_{1-x}Ni_xO_3$ at room temperature. Blue lines represent *Pnma* space group and red lines represent $R\bar{3}c$ space group.

Table 3.3: Band positions and assignment of the Raman modes[40–42]

$LaCrO_3$ (*Pnma*)	**$LaCrO_3$** ($R\bar{3}c$)	**Symmetry**	**Assignment**
124	125	B_{2g}	La and O oscillation along z axis
-	160	E_g	La oscillation
596	590	B_{3g}	O oscillation
256	-	A_g	$[BO_6]$ x rotations
411	-	B_{2g}	$[BO_6]$ out of phase bending
442	-	A_g	$[BO_6]$ bending

3.3 Discussion

In the calculation of the theoretical tolerance factor for the synthesized series, the ionic radius was employed (**Table 3.4**). It's noteworthy that the spin state of metal ions can affect their ionic radius, and thus calculations were performed for both low spin and high spin conditions. As depicted in **Figure 3.7a,b**, the resulting tolerance factors ranged between 0.90 to 0.96. Prior studies indicate that a tolerance factor between 0.95 and 1.0 typically leads to a cubic perovskite structure.[36,43] When the tolerance factor falls below 0.95, the atoms are packing too tightly, leading to structural distortion and a shift from the cubic structure to an orthorhombic or rhombohedral structure. The calculated tolerance factor values aligned well with the space groups obtained from Rietveld refinement (**Table 3.1**), with one notable exception. The $LaCr_{0.1}Co_{0.9}O_3$ and $LaCoO_3$ samples, exhibiting a low spin state of Co^{3+}, showed tolerance factors slightly greater than 0.95 yet adopted the $R\bar{3}c$ structure.

Table 3.4: Ionic radius table[27]

atom	charge	coordination	spin state	ionic radius(Å)
La	3+	9 ($R\bar{3}c$)	-	1.216
La	3+	8 ($Pnma$)	-	1.16
Cr	3+	6	-	0.615
Co	3+	6	low spin	0.545
Co	3+	6	high spin	0.61
Ni	3+	6	low spin	0.56
Ni	3+	6	high spin	0.6
O	2-	6	-	1.40

For the $LaCrO_3$ perovskite without doping, the tolerance factor (t) equals 0.90, indicating a relatively large B-site atom that prevents an ideal cubic perovskite structure. With both Co^{3+} and Ni^{3+} having smaller ionic radii than Cr^{3+}, increasing the doping concentration leads to a less substantial distortion of the lattice,

resulting in an increase in the tolerance factor with higher doping content. Notably, the tolerance factor (t) increases faster in the low spin situation and shows slower increments in the high spin scenario due to variations in ion radii.

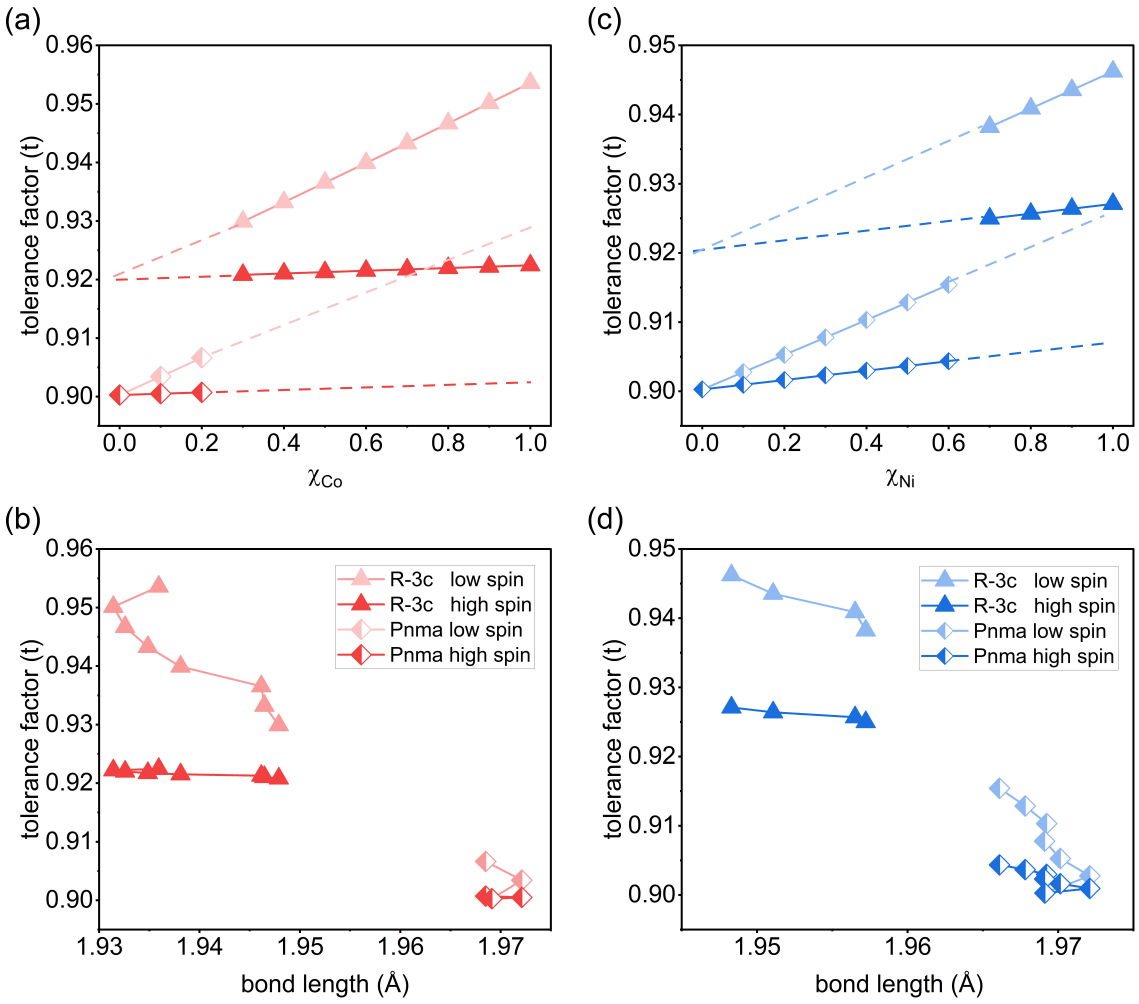

Figure 3.7: Tolerance factor analysis of (a) $LaCr_{1-x}Co_xO_3$ and (b) $LaCr_{1-x}Ni_xO_3$ series. Correlations between tolerance factor and bond length for the (c) Co-doped series and the (d) Ni-doped series.

The tolerance factor serves as a significant indicator of lattice stability and distortion. Regardless of low or high spin assumptions, the tolerance factor consistently increases with rising χ_j. This trend align well with the distortion within the $[BO_6]$ polyhedron due to B-O-B bond bending, which is evident as the χ_j increment correlates with an increase in the B-O-B bond angle (**Figure 3.5c**). Within the unit cell, the $R\bar{3}c$ structure demonstrates a higher symmetry compared to the *Pnma* structure due to the regular octahedra configuration of $[BO_6]$.

Correlations exist between the tolerance factor and phase transitions in both Co-doped and Ni-doped samples. The $R\bar{3}c$ structure indicates a tolerance factor above 0.92 with a B-O bond length below 1.96Å. As the B-O bond length surpasses 1.965Å, the tolerance factors decrease below 0.92, shifting the perovskite structure to the *Pnma* space group (**Figure 3.7b,d**). Notably, the threshold for this phase transition varies with different doping. In the Co-doped series, the bond length shifts from around 1.95Å to 1.97Å during the space group change. Comparatively, in the Ni-doped series, this transition occurs within a narrower gap, shifting from around 1.957Å to 1.966Å.

The systematic distortions of [BO_6] polyhedra are expected to influence electrochemical performance. As shown in **Figure 3.8**, the bending of the B-O-B bond reduces the overlapping of the 3*d* orbital of B-site metals and the oxygen 2*p* orbitals, which should lead to the reduction of covalency and thus effect perovskite's catalytic performance.[36,37,43,44]

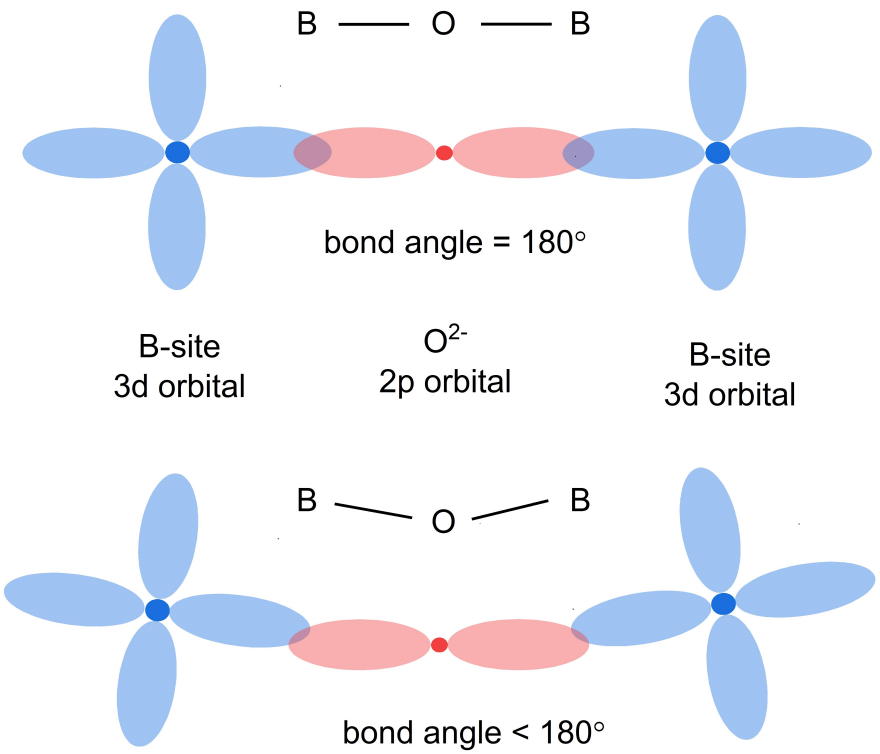

Figure 3.8: Schematic representation of electron cloud overlap in B-O-B bonds at varied bond angles

3.4 Summary

The two perovskite series $LaCr_{1-x}Co_xO_3$ and $LaCr_{1-x}Ni_xO_3$ were prepared using an adapted sol-gel method, resulting in single-phase compositions. The introduction of B-site doping has notable effects on the lattice space group, unit cell parameters, and B-O bond interactions. As the doping concentration increased, the samples undergo a structural transition from the *Pnma* to the $R\bar{3}c$ phase at different doping levels, accompanied by a consistent contraction of the lattice along all three lattice axes. The increments in B-O-B bond angles exhibit distinct stages, which are associated with the space group and doping concentration. Additionally, higher B-site doping led to a decreasing trend in B-O bond distances. The highly symmetric nature of the $[BO_6]$ polyhedron limits the information obtained through experimental Raman analysis regarding the B-site. These structural modifications induced by doping give rise to variations in B-O bond covalency, impacting the electrochemical performance as catalysts. In summary, the synthesized perovskite series undergo structural transitions from *Pnma* to $R\bar{3}c$ with increasing doping concentrations, resulting in changes in lattice parameters, B-O bond interactions, and B-O-B bond angles, while also affecting electrochemical performance as catalysts.

Chapter 4

Electrochemical Analysis

4.1 Introduction

The oxygen reduction reaction is a fundamental process in electrochemistry with significant implications in various applications. In alkaline environment, ORR can follow either a four-electron pathway, leading to the direct reduction of oxygen to hydroxide ions without any side products, or a two-electron pathway, resulting in the formation of H_2O_2. The four-electron pathway is particularly efficient in terms of oxygen utilization and is commonly employed as the positive electrode reaction in energy conversion and storage systems, such as metal-air batteries and alkaline fuel cells.[45–47] Previous research have reported ABO_3 perovskite oxides catalytic activity towards both the two-electron and the four-electron pathways.[13] These materials offer a cost-effective and potentially more durable alternative to traditional metal or metal alloy catalysts that include platinum (Pt).[48] The two-electron pathway, on the other hand, produces H_2O_2, a valuable clean oxidizing agent widely used in chemical and medical applications, as well as in the manufacturing industry and everyday life.[9–12] Electrochemical production offers a means of continuous on-site generation of H_2O_2. Notably, only a few heterogeneous electrocatalysts are capable of electrochemically producing H_2O_2, with a prominent subset being specific ABO_3 type perovskite oxides like $CaSnO_3$[22] and $SmCoO_3$.[49]

In the context of this research, the focus has been on studying the electrochemical performance of $LaCr_{1-x}Co_xO_3$ and $LaCr_{1-x}Ni_xO_3$ perovskites. The investigation delves into understanding how doping type, concentration, and catalyst structure influence the catalytic performance in ORR. Such studies are pivotal in optimizing catalyst design for specific electrochemical applications, offering pathways to enhance the efficiency and selectivity of ORR processes, whether the aim is to maximize energy conversion in fuel cells or to produce valuable chemical intermediates like H_2O_2.

4.2 Results

4.2.1 Baseline measurements and voltage selection for RRDE measurements

A comprehensive series of linear sweep voltammetry (LSV) experiments was conducted using both polished Pt and glassy-carbon (GC) electrodes to establish baseline signals and critical voltage parameters for subsequent electrochemical analyses. All measurements were performed in a 0.1 M KOH electrolyte under three distinct conditions for comparative purposes.

The LSV sweep on the Pt electrode primarily focused on analyzing reactions occurring on the Pt ring electrode, which is positioned around the GC disk electrode in a RRDE setup. As depicted in **Figure 4.1a**, reactions at the Pt electrode exhibited differences in current under various conditions. The blue line represents the inert condition, where negligible current was observed in the N_2 saturated environment. The observed cathodic currents, ranging from 0 V to 0.9 V, in the presence of H_2O_2 in saturated N_2, are indicative of the reduction of H_2O_2, while the anodic currents suggest the oxidation of H_2O_2. Measurements in an O_2 purged environment revealed a consistent anodic current in the ORR region and negligible current in the OER region, providing a background signal for ring current analysis. The introduction of H_2O_2 led to an increased steady-state current in the ORR region at around 0.7 V

and the appearance of an anodic plateau in the OER region. The current density difference between the O_2 saturated and H_2O_2 saturated conditions in the anodic and cathodic current plateaus is approximately the same, which correspond to the theoretical expectations. As discussed in the introduction section, the RRDE setup facilitates the transfer of products generated at the central disk electrode to the outer ring electrode, a process driven by centrifugal forces due to rotation. By setting the Pt ring electrode to a potential of 1.2 V, it becomes capable of detecting H_2O_2 generated at the disk electrode with minimal interference from O_2 related current.

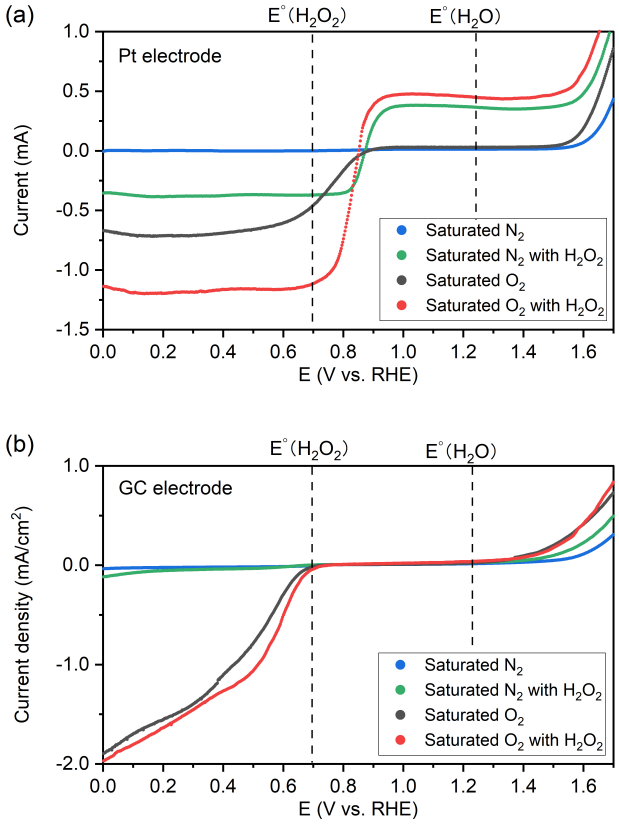

Figure 4.1: The LSV measurements at different environments on (a) the platinum ring electrode without coating. (b) The Glassy-Carbon disk electrode without coating. Data was collected with a rotation rate of 1500 r.p.m and a scan rate of 50mV/s.

.

As illustrated in **Figure 4.1b**, electrochemical reactions at the GC electrode exhibited a significant suppression under N_2 saturation conditions compared to those in an O_2 saturated electrolyte. A slowdown in the growth rate of the cathodic current

around 0.2 V was observed, indicating a deviation from the typical ORR current pattern, as depicted by the black line in **Figure 4.1a**. This variation suggests the influence of H_2O_2. Notably, the current density difference between the two O_2 saturated conditions is approximately the same, which aligns with the theoretical expectations.

4.2.2 Cyclic Voltammetry Analysis

Cyclic voltammetry (CV) measurements were performed prior to the LSV analyses. These CV measurements served not only to confirm the successful catalyst coatings but also to provide initial insights into the catalytic capabilities of the samples. CV measurements for selected samples are presented in **Figure 4.2a,b**. The oxygen reduction peaks for all samples, located within the potential range of 0.40 V to 0.58 V, indicate that the oxygen reduction reaction occurred. The pronounced cathodic oxygen reduction peaks observed signify the catalytic potential of both doped series in the ORR reactions. The absence of anodic peaks suggests that the reduction process is irreversible, as expected for a catalytic reaction.

In the case of Co-doped samples with varying structures, the peak cathodic potential (E_{pc}) initially increased, then shifted to higher potentials as the doping level increased (**Figure 4.2c**). For the Ni-doped series, the peak position consistently shifted negatively with an increase in doping amount, albeit accompanied by notable fluctuations. Comparatively, Co-doped samples exhibited overall higher reduction peak potentials than Ni-doped samples, suggesting that Co doping positively influences the catalysts' oxygen adsorption and desorption capabilities. No significant potential shifts were observed when the catalyst structure varied from *Pnma* to $R\bar{3}c$, indicating that structural differences might not significantly affect the oxygen reduction potential. The trend for current density change at the reduction peak position generally follows the E_{pc} change (**Figure 4.2d**). It is important to note that for both Co-doped and Ni-doped samples, there was a marked increase in current density at a doping concentration of 0.7. The Co-doped series with the *Pnma* structure demonstrated a higher current density compared to the $R\bar{3}c$ structure. In

contrast, the current density differences for the Ni-doped series were minimal, with the notable exceptions being undoped $LaCrO_3$ and $LaCr_{0.7}Ni_{0.3}O_3$.

Regarding OER reaction, a generally low current density was noted, with two exceptions: $LaCr_{0.8}Co_{0.2}O_3$ and $LaCr_{0.6}Ni_{0.4}O_3$, both of which exhibited significantly higher current densities, as shown in **Figure A.1**. This observation suggests a potential correlation between the samples' catalytic activity and specific doping concentrations.

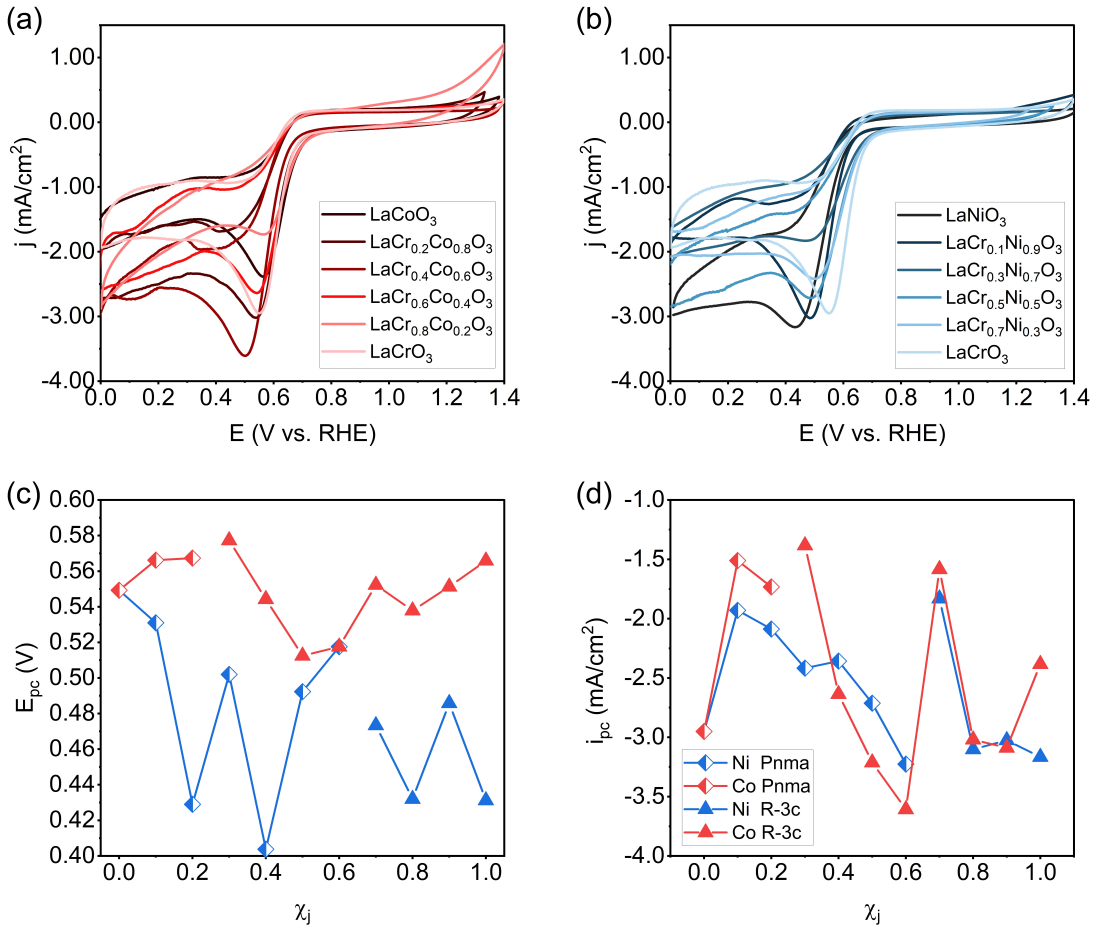

Figure 4.2: Cyclic voltammetry measurements for (a) selected $LaCr_{1-x}Co_xO_3$ samples (b) selected $LaCr_xNi_{1-x}O_3$ samples. (c) Oxygen reduction potential of both series. (d)Oxygen reduction peak current density of both series. Current density is calculated by using the collected current data divided by the area of the disk electrode.

4.2.3 Oxygen Reduction Reaction Analysis

The LSV for the ORR in the voltage range of 0 V to 1V was utilized to evaluate the catalytic activity of perovskites towards ORR. The disk current (i_{disk}), measured on the GC round electrode at the center of the RRDE, primarily reflects the ORR activity. Concurrently, the ring current (i_{ring}) was monitored on the Pt ring electrode, which was set to a potential of 1.2V based on prior voltage selection tests (**Figure 4.1**). Example ORR current data obtained using the RRDE setup are displayed in **Figure 4.3a**.

A typical characteristic observed in the ORR current profile is a increase in cathodic currents at around 0.6V on the disk electrode, which lead to a plateau. This is indicative of ORR electrcatalysis. The onset voltage is well aligned with the thermodynamic voltage for reduction of O_2 to H_2O_2. Notably, the nature of doping significantly affects the height of this plateau, the onset potential, and the measured ring current of the ORR reactions. This indicates the influence of doping on the efficiency and kinetics of the ORR process. The presence of the two-electron ORR reduction mechanism in the reaction is corroborated by i_{ring}. Setting the ring voltage to 1.2V ensures that the ring electrode is capable of oxidizing all the H_2O_2 generated during the ORR to O_2. This capability to detect and quantify H_2O_2 production provides valuable insights into the partial reduction processes occurring on the disk electrode and highlights the nuanced effects of different doping materials on the catalytic activity of perovskites in ORR.

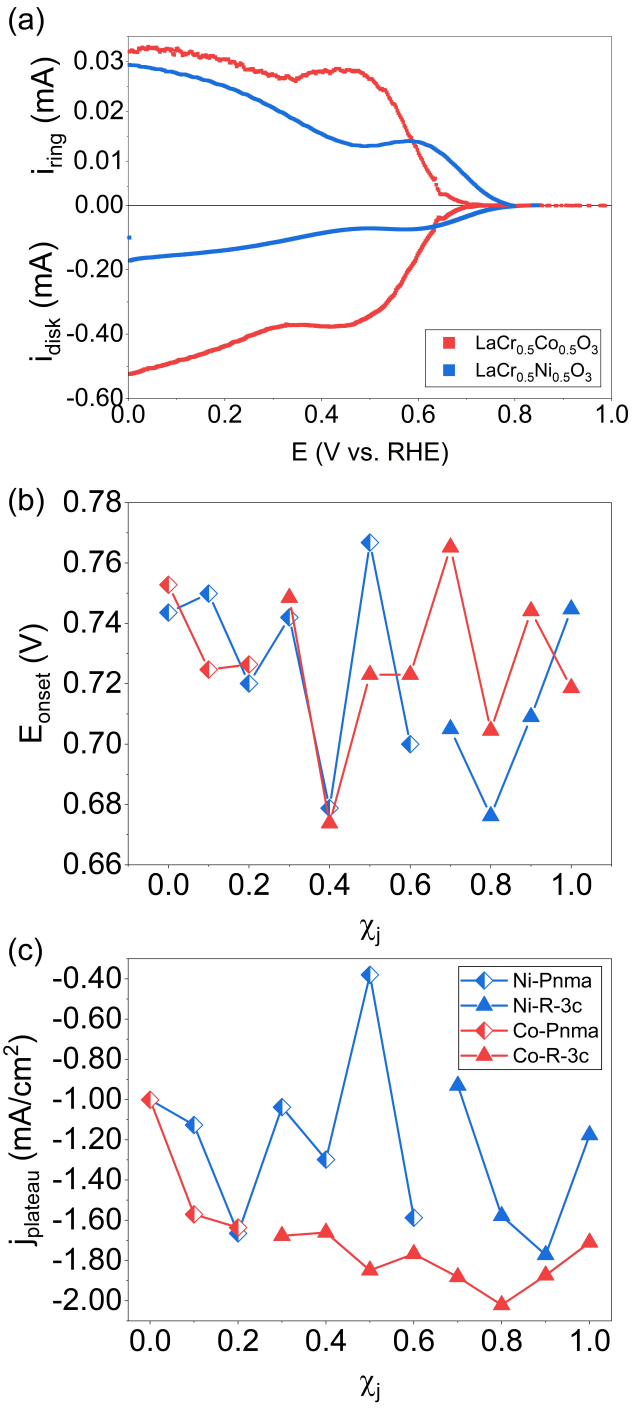

Figure 4.3: Oxygen reduction reaction analysis of (a) Disk and ring current of $LaCr_{0.5}Co_{0.5}O_3$ and $LaCr_{0.5}Ni_{0.5}O_3$.(b) Onset potential of the two series. (c) Current density of plateau of the two series.

.

In the study of various samples, the onset potential (E_{onset}) was observed to range between 0.67 V and 0.77 V, as depicted in **Figure 4.3b**. The E_{onset} was

identified at the voltage where a notable increase in ring current occurs, signifying the commencement of H_2O_2 generation. This range of onset potentials did not show a clear correlation with either the doping concentration or the space group of the perovskites.

In contrast, the plateau current density, $j_{plateau}$, exhibited marked differences when comparing the Co-doped series to the Ni-doped series. For the Co-doped series, $j_{plateau}$ typically ranged from about -1.6 to -2.0 mA/cm^2, as shown in **Figure 4.3c**. Furthermore, a general trend of decreasing current density with an increase in Co doping concentration was observed, suggesting a potential link between the Co doping level and the number of electrons transferred during the ORR. This trend might indicate a shift from the two-electron process towards a four-electron process. Conversely, the Ni-doped series exhibited plateau current densities between -0.4 to -1.7 mA/cm^2, which are notably lower than those in the Co-doped series. This disparity underscores the significant impact of the doping element on the ORR process.

The Tafel equation was used to derive kinetic information about the perovskite catalyst ORR reaction. The Tafel slope is calculated from the linear sections of the log value of current density versus potential plots. In **Figure 4.4a**, the Tafel plots for $LaCr_{0.5}Co_{0.5}O_3$ and $LaCr_{0.5}Ni_{0.5}O_3$ show a distinct linear regions in the low overpotential region ranges from approximately 52 mV/dec to 68 mV/dec.

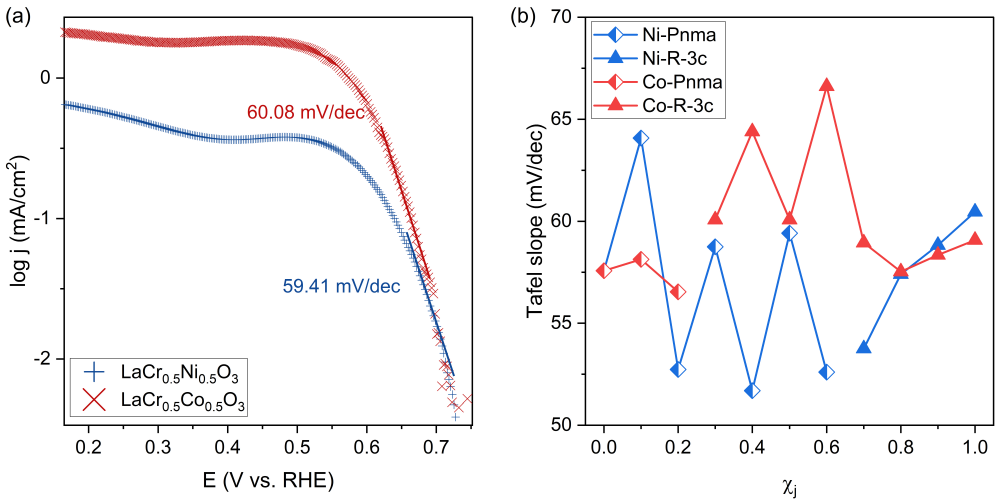

Figure 4.4: Tafel slope analysis of $LaCr_{1-x}Co_xO_3$ and $LaCr_xNi_{1-x}O_3$ series. (a) Examples of the calculation of Tafel slope value. (b) Summary of Tafel slopes for two sample series.

As depicted in **Figure 4.4b**, the Co-doped series exhibit lower Tafel slopes than the Ni-doped series across doping concentrations ranging from 0.2 to 0.8. This trend indicates that Co-doped perovskite catalysts are more efficient for the ORR in this concentration range, as they achieve higher current densities in a given voltage range. For the Ni-doped series with a *Pnma* structure, the Tafel slope values exhibit fluctuations with increasing doping concentration. Meanwhile, for the Ni-series series in the $R\bar{3}c$ structure, there is an observed increasing trend in Tafel slope values concurrent with the rise in doping concentration.

4.3 Discussion

The Tafel slope value is an indicator of the reaction mechanism happend during the ORR. The observed Tafel slope at around 60 mV/dec can be explained by the path shown in **Table 4.1**,[50] which proposed a possible mechanism for the 2-electrons steps. It shows that the adsorption of H_2O to the MO^- is the rate limiting step during the ORR.

Table 4.1: A proposed mechanism for the two-electrons pathway for ORR[50]

rate-determining step	Theoretical Tafel slope value (mV/dec)
$O_2 + 2M \rightarrow MO$	15
$MO + e^- \rightarrow MO^-$	40
$MO^- + H_2O \rightarrow MOH + OH^-$	60
$MOH + e^- \rightarrow M + OH^-$	120

The analysis of disk and ring currents in RRDE experiments is instrumental in determining the number of electrons transferred during the ORR reaction. This electron transfer number, N_d, is a crucial indicator of the reaction's completeness and can be calculated using the currents from both the disk electrode (i_d) and the ring electrode (i_r) using the following equation:[51]

$$N_\mathrm{d} = 4 * \frac{i_\mathrm{d}}{i_\mathrm{d} + \frac{i_\mathrm{r}}{N}} \tag{4.1}$$

In this equation, N represents the collection efficiency of the RRDE. In this project, it was used as the same as the theoretical efficiency, 24.9%, as calculated form the electrode efficiency measurements (**Figure A.2**). A fully completed ORR involves the transfer of four electrons. In contrast, a two-electron step, indicative of incomplete ORR leading to H_2O_2 formation, signifies that only two electrons are involved.

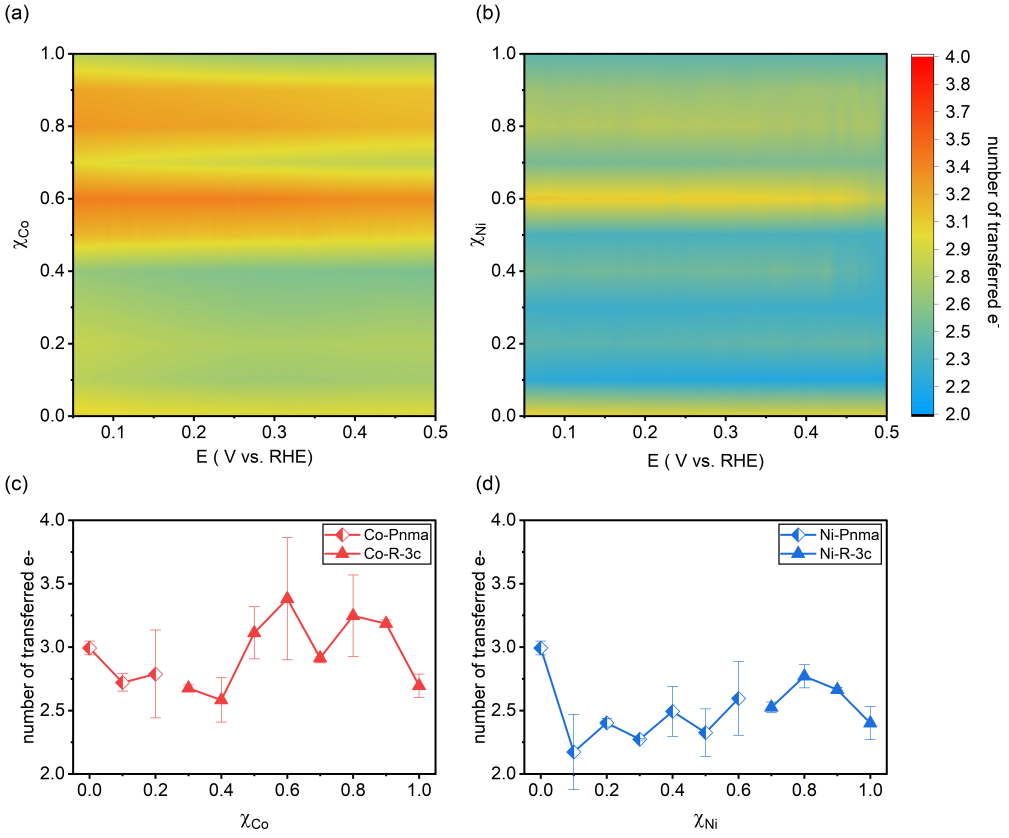

Figure 4.5: The calculated number of transferred electrons of (a) $LaCr_{1-x}Co_xO_3$ and (b) $LaCr_xNi_{1-x}O_3$ during ORR reaction. (c) The average number of transferred electrons of Co-dope series. (d) The average number of transferred electrons of Ni-dope series. Y error calculated as the standard deviation of multi measurements' results of the same sample.

The number of electrons transferred during the ORR process for different catalysts is shown in **Figure 4.5**. Notably, the Ni-doped series demonstrates fewer electrons being transferred compared to the Co-doped series, suggesting that the presence of Ni may hinder the completion of the ORR, favoring the production of H_2O_2. This observation is consistent with the LSV measurements (**Figure 4.3c**), where the Ni-doped series exhibited a $j_{plateau}$ higher than the Co-doped series. Con-

versely, the Co-doped series showcases a stronger tendency to catalyst the reaction towards the four-electrons pathway (**Figure 4.5c**). The influence of perovskite structure on catalytic activity is noticeable: for Co doping concentrations ranging from 0 to 0.4, corresponding to the *Pnma* space group, the catalysts promote a hybrid of both four-electron and two-electron ORR processes. As the χ_{Co} value increases from 0.6 to 1.0, the average transferred electrons are closer to 4, indicating a stronger selectivity for the four-electron ORR process.

In the preceding two chapters, the structural changes and electrochemical behavior of doped perovskite oxides were discussed. This section will delve into the interplay between structural features and catalyst performance in these materials.

The relationship between the B-O bond length and the average number of electrons transferred during the ORR is shown in **Figure 4.6a**. Previous studies have found that stronger covalency in B-O bond facilitates oxygen species exchange on the surface of B-site ions, thus improving the complete four-electron ORR process.[20] Stronger covalency is indicated by shorter B-O bonds.[52] The experimental trend observed in this study corresponds with these findings, indicating a negative relationship between bond length and the number of transferred electrons. An increase in bond length leads to a weaker B-O bond, which, in turn, facilitates the desorption of the formed OOH^- species from the catalyst surface, thereby promoting the formation of H_2O_2. It is evident that the structural configuration of the catalysts influences ORR selectivity. Catalysts with the *Pnma* structure, characterized by longer B-O bonds, typically exhibit a lower number of electrons involved in the reaction compared to those with the $R\bar{3}c$ structure within the same doping series. Notably, the fluctuation between odd and even doping numbers in the Ni-doped series is observed, which does not seem to be directly attributable to bond length variations.

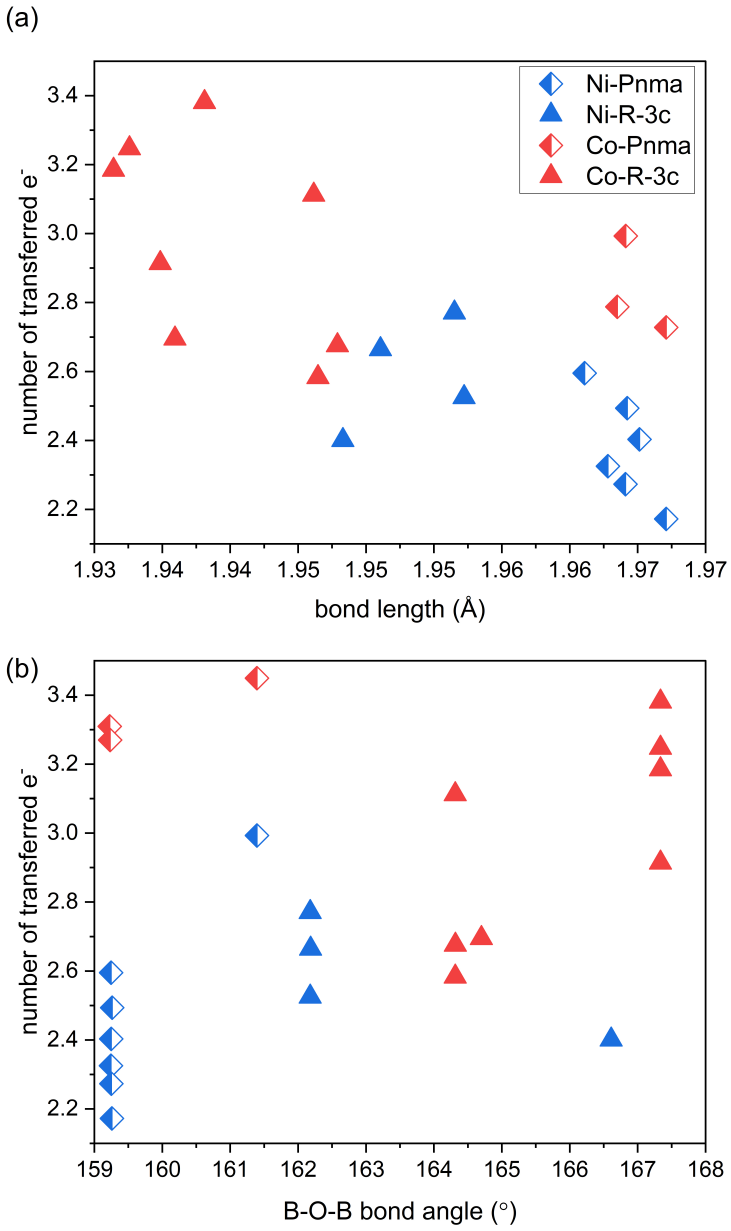

Figure 4.6: The correlations between lanthanum perovskite oxides (a) B-O bond length and (b) B-O-B bond angle with their ORR catalytic activity.

The B-O-B bond angle reflects the degree of hybridization between the B-site $3d$ orbitals and the oxygen $2p$ orbitals. In an ideal [BO_6] octahedron, the $3d$ B-site metal orbital and $2p$ oxygen orbital engage in a 'head-on collision' mode, with the B-O-B bond angle around 180°.[37] As depicted in **Figure 3.8**, bending of the B-O-B bond, leading to a decrease in the B-O-B bond angle, decreases the overlap between the $3d$ and $2p$ orbitals. This reduction negatively affects electron transfer within the

lattice and lowers the electrocatalytic activity towards completing the ORR.[37] This trend is shown in **Figure 4.6b**. Similar to the bond length analysis, the correlation between structural characteristics and ORR selectivity is more pronounced in the Co-doped series. A general trend is observed where an increase in the B-O-B bond angle leads to a corresponding increase in the number of electrons transferred. In contrast, the Ni-doped series exhibits a more complex pattern, with fluctuations in catalytic activity that make discerning a clear trend challenging.

The XAS results suggest that changes in the oxidation state might be a key factor influencing the differing ORR selectivity between the Co-doped and Ni-doped series. As demonstrated in **Figure 4.7a**, the normalized Co K edge peaks of selected Co-doped samples have no significant variation across different doping concentrations. These edge energies are indicative of a Co 3+ state, as corroborated by prior research on Co oxidation states.[53,54] In contrast, the Ni-doped samples exhibit different Ni edge energies (**Figure 4.7b**). The normalized edge energy for Ni shifts positively as doping concentration increases from 0.1 to 0.8, followed by a negative shift from 0.8 to 1.0. This shift suggests a change in the oxidation state of Ni between 2+ and 3+ state within the selected samples.[55] This could be attributed to the alteration in the electron configuration at the B-site, prompted by varying Ni concentrations. The phase transition from *Pnma* to $R\bar{3}c$ and the possible oxygen vacancies within the lattice may also contribute to these oxidation state changes. Overall, the XAS results are in line with the hypothesis that the incorporation of Cr and Ni at the B-site in perovsktie oxide leads to different electron configuration in the split *d* orbitals, thereby impacting the catalytic performance of the samples.

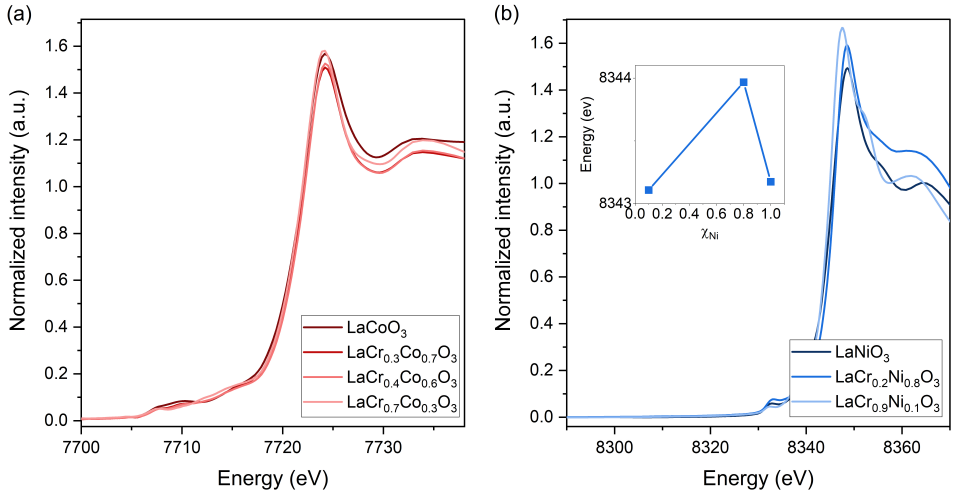

Figure 4.7: The XAS results of selected (a) Co-doped samples. (b) Ni-doped samples. The inset shows the relationship between the Ni edge energy and Ni doping concentration.

4.4 Summary

The experimental investigations utilizing the RRDE technique have provided critical insights into the electrochemical behaviors of various catalysts. Through CV measurements, distinct redox characteristics were observed, which were significantly influenced by the composition of the catalyst. Notably, the results indicated that the catalytic activity for the OER was not particularly pronounced. More specifically, the electrochemical kinetic analysis for the ORR revealed that the inclusion of Co in perovskite oxides enhances their selectivity atowards a complete ORR process. This indicates that Co-doped samples favor the four-electron pathway of the ORR, leading to the efficient reduction of oxygen to water. On the other hand, the introduction of Ni was found to increase the selectivity towards the generation of H_2O_2, a characteristic of the two-electron reduction pathway in ORR. This suggests that Ni doping facilitates a partial reduction of oxygen, resulting in the production of H_2O_2. These observations highlight the crucial influence of dopant type and perovskite structure on the selectivity and efficiency of catalyzed ORR processes. The ability to tailor the ORR pathway through strategic doping presents a valuable approach for designing and optimizing catalysts for specific electrochemical applications.

Chapter 5

Conclusions and Outlook

5.1 Conclusions

In summary, this thesis investigated how the lattice structure of lanthanum chromium oxide perovskites changes with varying concentrations of Co and Ni doping, alongside their electrochemical catalytic behavior towards the oxygen reduction reaction.

The $LaCr_{1-x}Co_xO_3$ and $LaCr_{1-x}Ni_xO_3$ samples exhibited a structural transition from the *Pnma* to the $R\bar{3}c$ phase as the concentration of B-site doping increased. This correlation between doping concentration and changes in lattice parameters aligns well with tolerance factor analysis. With an increase in doping concentration, there is a noticeable decrease in the distortion of the perovskite lattice. Concurrently, the lattice exhibits a trend of contraction along the defined a and c axes. The bond angles and lengths within the $[BO_6]$ polyhedra in the lattice are also influenced by the type and concentration of doping.

Electrochemically, the analysis revealed that the catalytic activity for the oxygen evolution reaction was not particularly pronounced in the synthesized catalyst series. However, for the ORR, the samples exhibited variations in catalytic activity based on the type and concentration of doping. The Co-doped series tended to increase the selectivity of the ORR towards the four-electron pathway, while the presence of Ni indicated a tendency to catalyze the ORR towards the two-electron pathway. The

Tafel slope values, ranging from 52 mV/dec to 68 mV/dec, provide insights into the ORR mechanism, suggesting that the rate-determining step involves the adsorption of H_2O. The XAS analysis indicates that the oxidation states of the B-site atoms might be a key factor affecting the samples' catalytic performance.

5.2 Outlook

The project revealed notable variations in the catalytic activity within the Co-doped and Ni-doped perovskite oxide series. The selection of B-site doping elements could extend beyond Cr, Co, and Ni to include a broader range of 3d transition metals, enabling a more comprehensive investigation. Such an expansion could significantly enhance our understanding of the relationship between the structural attributes of perovskite oxides and the corresponding changes in their catalytic activity. Through extended research, it would be possible to identify the most effective combinations and ratios of B-site elements for optimizing both the four-electron and two-electron oxygen reduction reactions.

The intrinsic structural reasons behind the fluctuating ORR catalytic activity in the Ni-doped series, have not yet been fully understood. Further XAS analysis of the entire sample series will provide detailed structural information about the perovskite oxide samples. This comprehensive analysis could pinpoint specific structural characteristics responsible for the observed variations in catalytic activity. Additionally, it can offer valuable insights into the presence of oxygen vacancies within the lattice, a crucial factor influencing ORR catalyst performance.

Looking forward, other key aspects should also be studied, including the catalytic stability and the development of synthesis methods suitable for large-scale production, which are critical for discovering efficient catalysts for the different pathways in the ORR.

References

(1) Borup, R. L.; Kusoglu, A.; Neyerlin, K. C.; Mukundan, R.; Ahluwalia, R. K.; Cullen, D. A.; More, K. L.; Weber, A. Z.; Myers, D. J. *Current Opinion in Electrochemistry* **2020**, *21*, Energy Storage Energy Transformation, 192–200.

(2) Fuel cell partnership, H. Fuel Cell Electric Vehicle Sales: 2012-2023 https://h2fcp.org/sites/default/files/FCEV-Sales-Tracking.pdf (accessed 11/26/2023).

(3) Khorshidian, M; Sedighi, M. *Hydrogen, Fuel Cell amp; Energy Storage* **2019**, *6*, 91–115.

(4) Ramachandran, R.; Chen, T.-W.; Veerakumar, P.; Anushya, G.; Chen, S.-M.; Kannan, R.; Mariyappan, V.; Chitra, S.; Ponmurugaraj, N.; Boominathan, M. *RSC Adv.* **2022**, *12*, 28227–28244.

(5) Gasteiger, H.; Panels, J.; Yan, S. *Journal of Power Sources* **2004**, *127*, Eighth Ulmer Electrochemische Tage, 162–171.

(6) Nie, Y.; Li, L.; Wei, Z. *Chem. Soc. Rev.* **2015**, *44*, 2168–2201.

(7) Li, H.; Kelly, S.; Guevarra, D.; Wang, Z.; Wang, Y.; Haber, J. A.; Anand, M.; Gunasooriya, G. T. K. K.; Abraham, C. S.; Vijay, S.; Gregoire, J. M.; Nørskov, J. K. *Nat Catal* **2021**, *4*, 463–468.

(8) Gunasooriya, G. T. K. K.; Kreider, M. E.; Liu, Y.; Zamora Zeledón, J. A.; Wang, Z.; Valle, E.; Yang, A.-C.; Gallo, A.; Sinclair, R.; Stevens, M. B.; Jaramillo, T. F.; Nørskov, J. K. *ACS Nano* **2022**, *16*, PMID: 35377139, 6334–6348.

(9) Hage, R.; Lienke, A. *Angewandte Chemie International Edition* **2006**, *45*, 206–222.

(10) Kosaka, K.; Yamada, H.; Shishida, K.; Echigo, S.; Minear, R. A.; Tsuno, H.; Matsui, S. *Water Research* **2001**, *35*, 3587–3594.

(11) Chidambara Raj, C.; Li Quen, H. *Chemical Engineering Science* **2005**, *60*, 5305–5311.

(12) Lane, B. S.; Burgess, K. *Chemical Reviews* **2003**, *103*, PMID: 12848577, 2457–2474.

(13) online, T. E. C. I. Hydrogen peroxide https://www.essentialchemicalindustry.org/chemicals/hydrogenperoxide.html (accessed 07/15/2023).

(14) newswire, G. Global Hydrogen Peroxdie Industry https://www.globenewswire.com/newsrelease/2020/07/22/2065580/0/en/Global-Hydrogen-Peroxide-Industry.html (accessed 07/15/2023).

(15) Campos-Martin, J. M.; Blanco-Brieva, G.; Fierro, J. L. G. *Angewandte Chemie International Edition* **2006**, *45*, 6962–6984.

(16) Solsona, B. E.; Edwards, J. K.; Landon, P.; Carley, A. F.; Herzing, A.; Kiely, C. J.; Hutchings, G. J. *Chemistry of Materials* **2006**, *18*, 2689–2695.

(17) Shi, X.; Back, S.; Gill, T. M.; Siahrostami, S.; Zheng, X. *Chem* **2021**, *7*, 38–63.

(18) Ji, Q.; Bi, L.; Zhang, J.; Cao, H.; Zhao, X. S. *Energy Environ. Sci.* **2020**, *13*, 1408–1428.

(19) Risch, M. *Catalysts* **2017**, *7*.

(20) Suntivich, J.; Gasteiger, H. A.; Yabuuchi, N.; Nakanishi, H.; Goodenough, J. B.; Shao-Horn, Y. *Nature Chem* **2011**, *1*, 546–550.

(21) Kulkarni, A.; Siahrostami, S.; Patel, A.; Nørskov, J. K. *Chemical Reviews* **2018**, *118*, PMID: 29405702, 2302–2312.

(22) Park, S. Y.; Abroshan, H.; Shi, X.; Jung, H. S.; Siahrostami, S.; Zheng, X. *ACS Energy Letters* **2019**, *4*, 352–357.

(23) Data, P. M. General Perovskite Information https://webmineral.com/data/Perovskite.shtml (accessed 11/27/2023).

(24) Phillip Szuromi, B. G. *Science* **2017**, *358*, 732–733.

(25) Ono, L. K.; Juarez-Perez, E. J.; Qi, Y. *ACS Applied Materials & Interfaces* **2017**, *9*, PMID: 28682587, 30197–30246.

(26) In *Perovskites*; John Wiley Sons, Ltd: 2016; Chapter 1, pp 1–41.

(27) Of Medicine, N. L. Atomic Radius in the Peridoic Table of Elements https://pubchem.ncbi.nlm.nih.gov/periodic-table/atomic-radius/ (accessed 07/15/2023).

(28) Reis, J. V.; Pereira, T. C.; Teles, T. H.; França, A. B.; Bellido, J. D. A.; Naves, F. L.; Baston, E. P. *Materials Letters* **2018**, *227*, 261–263.

(29) Whittingham, A. W. H.; Liu, X.; Smith, R. D. L. *ChemCatChem* **2022**, *14*, e202101684.

(30) Navas, D.; Fuentes, S.; Castro-Alvarez, A.; Chavez-Angel, E. *Gels* **2021**, *7*.

(31) Osman, N.; Abdul Samat, A.; Che Mat, A. N.; Abd Malek, N. I.; Andas, J. *Ceramics International* **2022**, *48*, 2289–2297.

(32) Toby, B. H.; Von Dreele, R. B. *Journal of Applied Crystallography* **2013**, *46*, 544–549.

(33) Lee, S.-J.; Pyun, S.-I.; Lee, S.-K.; Kang, S.-J. L. *Israel Journal of Chemistry* **2008**, *48*, 215–228.

(34) Peña, M. A.; Fierro, J. L. G. *Chemical Reviews* **2001**, *101*, PMID: 11710238, 1981–2018.

(35) Royer, S.; Duprez, D.; Can, F.; Courtois, X.; Batiot-Dupeyrat, C.; Laassiri, S.; Alamdari, H. *Chemical Reviews* **2014**, *114*, PMID: 25253387, 10292–10368.

(36) Xu, N.; Zhao, H.; Zhou, X.; Wei, W.; Lu, X.; Ding, W.; Li, F. *International Journal of Hydrogen Energy* **2010**, *35*, 7295–7301.

(37) Sun, Y.; Liu, Z.; Zhang, W.; Chu, X.; Cong, Y.; Huang, K.; Feng, S. *Small* **2019**, *15*, 1803513.

(38) Ashok, A.; Kumar, A.; Bhosale, R. R.; Almomani, F.; Malik, S. S.; Suslov, S.; Tarlochan, F. *Journal of Electroanalytical Chemistry* **2018**, *809*, 22–30.

(39) Wang, Y.; Cheng, H.-P. *The Journal of Physical Chemistry C* **2013**, *117*, 2106–2112.

(40) Silva, R.; Cunha, F.; Barrozo, P. *Solid State Communications* **2021**, *333*, 114346.

(41) Iliev, M.; Litvinchuk, A.; Hadjiev, V.; Wang, Y.-Q; Cmaidalka, J.; Meng, R.-L; Sun, Y.; Kolev, N.; Abrashev, M. *Physical Review B* **2006**, *74*, 214301.

(42) Iliev, M. N.; Abrashev, M. V. *Journal of Raman Spectroscopy* **2001**, *32*, 805–811.

(43) Li, Z.; Yang, M.; Park, J.-S.; Wei, S.-H.; Berry, J. J.; Zhu, K. *Chemistry of Materials* **2016**, *28*, 284–292.

(44) Silva, R.; Cunha, F.; Barrozo, P. *Solid State Communications* **2021**, *333*, 114346.

(45) Winter, M.; Brodd, R. J. *Chemical Reviews* **2004**, *104*, PMID: 15669155, 4245–4270.

(46) Lu, S.; Pan, J.; Huang, A.; Zhuang, L.; Lu, J. *Proceedings of the National Academy of Sciences* **2008**, *105*, 20611–20614.

(47) Dunn, B.; Kamath, H.; Tarascon, J.-M. *Science* **2011**, *334*, 928–935.

(48) Stevens, M. B. et al. *Energy Environ. Sci.* **2022**, *15*, 3775–3794.

(49) He, J.; Zhou, W.; Sunarso, J.; Xu, X.; Zhong, Y.; Shao, Z.; Chen, X.; Zhu, H. *Electrochimica Acta* **2018**, *260*, 372–383.

(50) Bockris, J. O.; Otagawa, T. *The Journal of Physical Chemistry* **1983**, *87*, 2960–2971.

(51) Zhou, R.; Zheng, Y.; Jaroniec, M.; Qiao, S.-Z. *ACS Catalysis* **2016**, *6*, 4720–4728.

(52) Wang, W.; Liu, W.; Kamiko, M.; Yagi, S. *New J. Chem.* **2022**, *46*, 13082–13088.

(53) Vats, A. K.; Kumar, A.; Rajput, P.; Kumar, A. *J Mater Sci: Mater Electron* **2022**, *33*, 12590–2606.

(54) Chou, S.-C.; Tso, K.-C.; Hsieh, Y.-C.; Sun, B.-Y.; Lee, J.-F.; Wu, P.-W. *Materials* **2020**, *13*.

(55) Ohnuma, T.; Kobayashi, T. *RSC Adv.* **2019**, *9*, 35655–35661.

Appendix A

Supplementary Information

Table A.1: Parameters used in the Rietveld refinement

Parameters
number of coefficient for baseline subtraction
Histogram scale factor
Sample displacement (μm)
Sample transparency ($1/\mu eff, cm$)
Refine unit cell
Phase fraction
Domain size (μm)

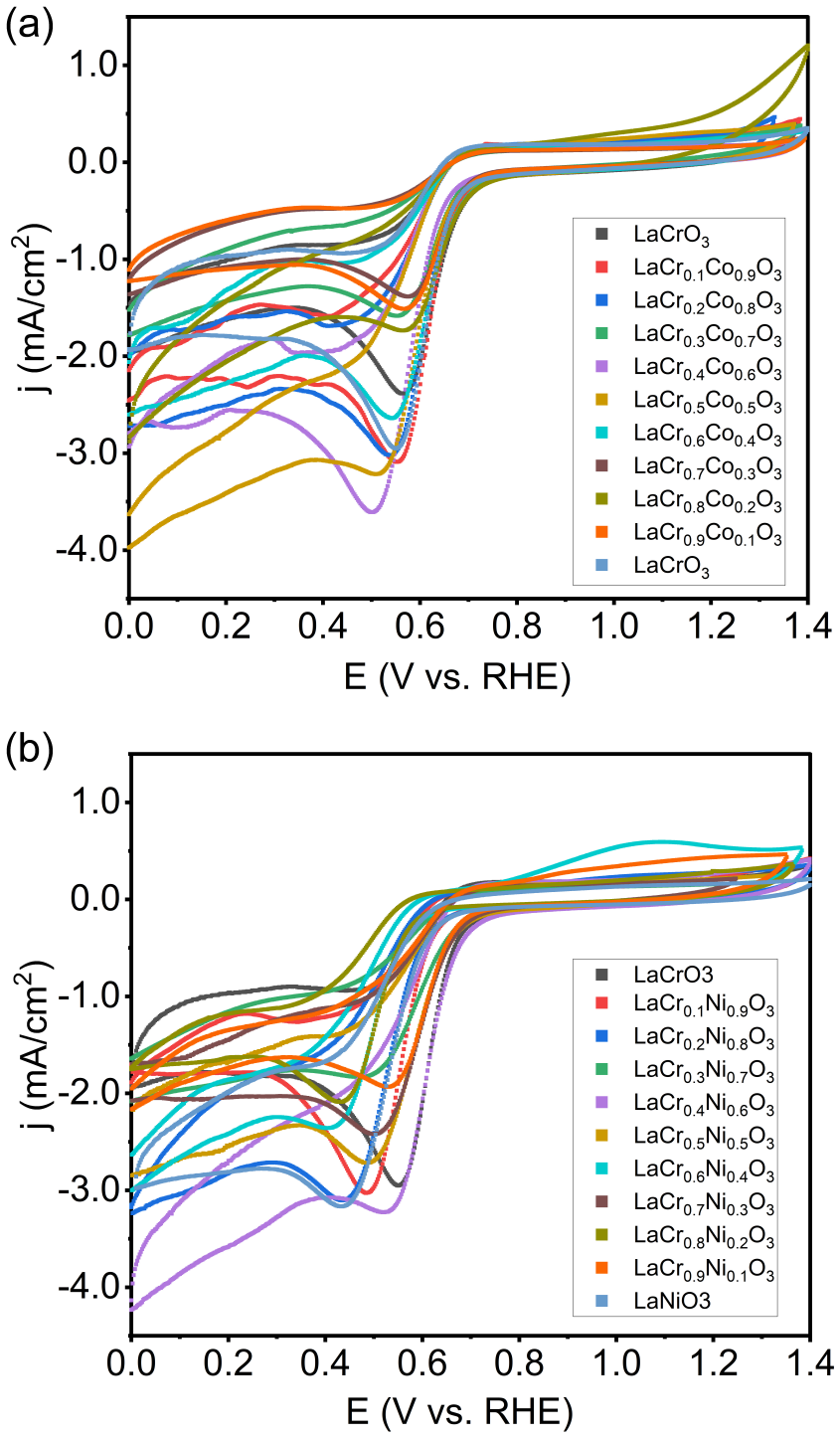

Figure A.1: Cyclic voltammatry measurements for all samples.

.

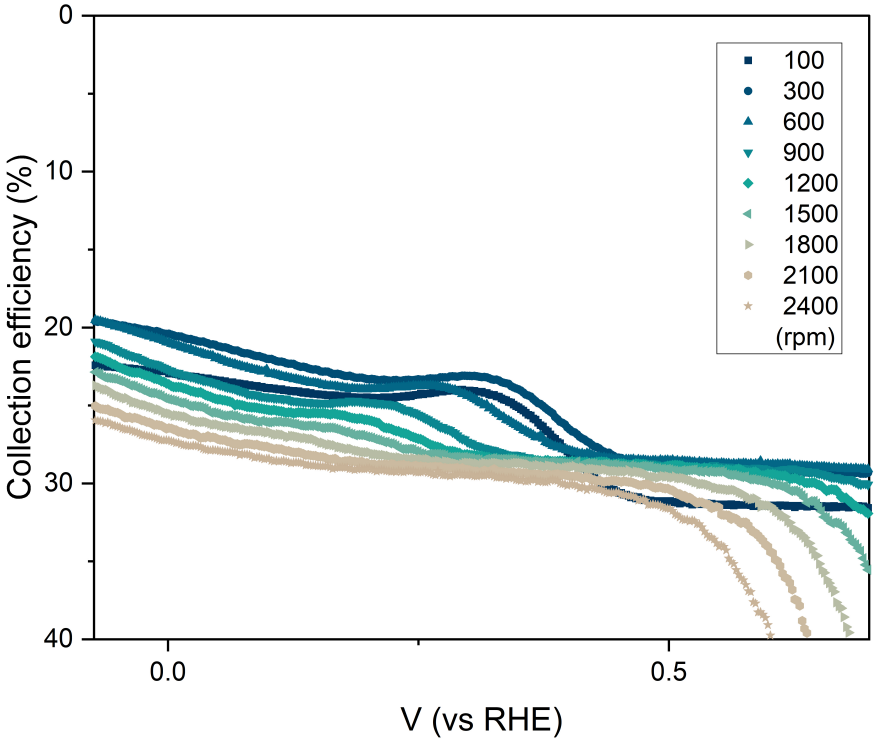

Figure A.2: The calculated collection efficiency of polished RRDE.